



Strong-field QED effects on polarization states in dipole and quadrudipole pulsar emissions

Dong-Hoon Kim^{1,2,a}, Chul Min Kim^{3,b}, Sang Pyo Kim^{4,5,c}

¹ The Research Institute of Basic Science, Seoul National University, 1 Gwanak-ro, Seoul 08826, Republic of Korea

² Department of Physics and Astronomy, Seoul National University, 1 Gwanak-ro, Seoul 08826, Republic of Korea

³ Advanced Photonics Research Institute, Gwangju Institute of Science and Technology, 123 Cheomdangwagi-ro, Gwangju 61005, Republic of Korea

⁴ Department of Physics, Kunsan National University, 558 Daehak-ro, Gunsan 54150, Republic of Korea

⁵ Asia Pacific Center for Theoretical Physics, POSTECH, 77 Cheongam-ro, Pohang 37673, Republic of Korea

Received: 10 September 2024 / Accepted: 27 November 2024 / Published online: 26 December 2024
© The Author(s) 2024

Abstract Highly magnetized neutron stars have quantum refraction effects on pulsar emission due to the non-linearity of the quantum electrodynamics (QED) action. In this paper, we investigate the evolution of the polarization states of pulsar emission under the quantum refraction effects, combined with the dependence on the emission frequency, for dipole and quadrudipole pulsar models; we solve a system of evolution equations of the Stokes vector, where the birefringent vector, in which such effects are encoded, acts on the Stokes vector. At a fixed emission frequency, depending on the magnitude of the birefringent vector, dominated mostly by the magnetic field strength, the evolution of the Stokes vector largely exhibits three different patterns: (i) monotonic, or (ii) half-oscillatory, or (iii) highly oscillatory behaviors. These features are understood and confirmed by means of approximate analytical solutions to the evolution equations. Also, the evolution patterns are shown to differ between dipole and quadrudipole pulsar models, depending on the magnetic field strength.

1 Introduction

Strong fields may open a window for testing fundamental physics. Even before quantum electrodynamics (QED) was fully developed and precisely tested in the weak field regime, Heisenberg and Euler showed that a strong electromagnetic field can polarize the Dirac vacuum [1]. Schwinger introduced the proper-time integral method to obtain the one-

loop effective QED action of the vacuum under a uniform electromagnetic field [2]. The so-called Heisenberg-Euler-Schwinger (HES) action provides an effective theory of electrodynamics in strong fields, in which the linear Maxwell vacuum is turned into a dielectric medium with electric, magnetic, and magneto-electric responses. Consequently, a photon propagating in a region of strong electromagnetic fields can experience vacuum birefringence, i.e., a quantum refraction effect [3,4]. Furthermore, when the electric field is sufficiently strong to be comparable to the critical electric field strength ($E_c = m_e^2 c^3 / (e\hbar) \approx 1.3 \times 10^{16}$ V/cm), electron-positron pairs can be created spontaneously out of the vacuum, which is called Sauter-Schwinger pair production [5–7]. Observing these effects will validate the quantum vacuum model in the strong-field regime; however, vacuum birefringence is practically far more likely to be implemented or observed than Sauter-Schwinger pair production.

Although the relevant field strength is too high to attain by terrestrial means, an experiment and several proposals for testing strong-field QED have been reported. In the PVLAS (Polarizzazione del Vuoto con Laser, i.e., polarization of vacuum with laser) project, permanent, superconducting magnets have been used with laser as a probe, and a limit on vacuum birefringence has been reported for a field strength of 2.5×10^4 G [8]. Recently, several proposals have appeared, in which ultra-intense laser fields are used with X-rays as a probe [9–11]; the current ultra-intense laser can provide a magnetic field strength of 10^{10} G [12], which corresponds to millisecond pulsars, but not to young pulsars. Although the fields from such lasers are still weaker than the critical magnetic field strength, $B_c = m_e^2 c^3 / e\hbar \approx 4.414 \times 10^{13}$ G by three orders, these proposals are promising for the obser-

^a e-mail: ki13130@gmail.com (corresponding author)

^b e-mail: chulmin@gist.ac.kr

^c e-mail: sangkim@kunsan.ac.kr

vation of vacuum birefringence in the relatively weak-field regime. Thus, they are seriously considered to be conducted at upcoming ultra-intense laser facilities [12].

However, the observation of vacuum birefringence in the strong-field regime requires a field strength comparable to the critical value. It has been predicted that such extreme fields are available from astrophysical compact objects. For instance, highly magnetized neutron stars have magnetospheres whose field strength approaches up to $\sim 2 \times 10^{15}$ G (about 50 times as high as the critical field strength) [3, 13]. In this regard, several space telescope missions are being conducted or proposed to observe the X-rays from neutron stars for vacuum birefringence: the Imaging X-ray Polarimetry Explorer (IXPE) [14], X-ray Polarimeter Satellite (XPoSat) [15], the enhanced X-ray Timing and Polarimetry (eXTP) [16] and the Compton Telescope project [17]. The X-rays from a neutron star contain information about vacuum birefringence in its magnetosphere, and the birefringence effect accumulates over the magnetospheric size. Such accumulation is a great advantage compared to terrestrial laser experiments, not to mention the available field strength. This way, astrophysical compact objects can be used as a laboratory to test fundamental physics in the strong-field regime [3, 18, 19].

The HES action is well approximated by the post-Maxwellian action, even up to the strength one order lower than the critical magnetic field B_c , which keeps up to the quadratic terms of the Maxwell scalar and pseudo-scalar. Therefore, the post-Maxwellian action exhibits non-linear characteristics of vacuum polarization, such as quantum refraction [20–22]. Previously, we have studied the quantum refraction effects on the propagation of a probe photon in the magnetic dipole field background of a pulsar model [23]. The study is non-trivial in comparison with other similar studies wherein the background magnetic field is assumed to be uniform, in that we have to deal with a dipole magnetic field, the strength and direction of which vary over space.

In this work, we investigate the evolution of the polarization states of pulsar emission under the quantum refraction effects, combined with the dependence on the emission frequency, for dipole and quadrupole (for the first time, to our knowledge) pulsar models; with growing theoretical and observational concerns for beyond-dipole effects, this study extends the scope of previous works by taking into account the multipolar magnetic field structure, the importance of which has been illuminated in different contexts of pulsar astronomy by a number of studies (see [24–28] and references therein). To this end, we employ the evolution equations of the Stokes vector, where such effects are encoded into the birefringent vector that acts on the Stokes vector. The Stokes vector has a crucial advantage over the polarization vector in representing polarization states: it can be directly determined from experimentally measurable quantities and accommodate depolarization effects due to incom-

plete coherence and random processes during the photon propagation. Solutions of the evolution equations describe how the polarization states change along the photon propagation path from the emission point towards an observer. It turns out that the evolution of the Stokes vector, at a fixed frequency of emission, largely exhibits three different patterns, depending on the magnitudes of the birefringent vector, dominated mostly by the magnetic field strength: (i) fractionally oscillatory - monotonic, or (ii) half-oscillatory, or (iii) highly oscillatory behaviors, which are found by numerical solutions and also confirmed by approximate analytical solutions. These are novel features rarely illuminated in previous studies on the same topic. In addition, it is investigated how the aforementioned features regarding the evolution of the Stokes vector change as we replace a dipole field with a quadrupole field to modify the pulsar magnetic field structure. Throughout our analysis, X-ray emission from pulsars, with frequency $\sim 10^{18}$ Hz, is considered; in this regime, the vacuum contribution to the birefringence dominates that of the plasma [29, 30]. Also, our analysis is sufficiently rigorous in solving the evolution equations of the Stokes vector, in that we feed into the equations the precise information of photon propagation under the pulsar rotation effect, through the magnetic field geometries of oblique dipole and quadrupole rotators, with all the quantities involved fully affine-parameterized; then, the equations are solved solely in terms of an affine parameter.

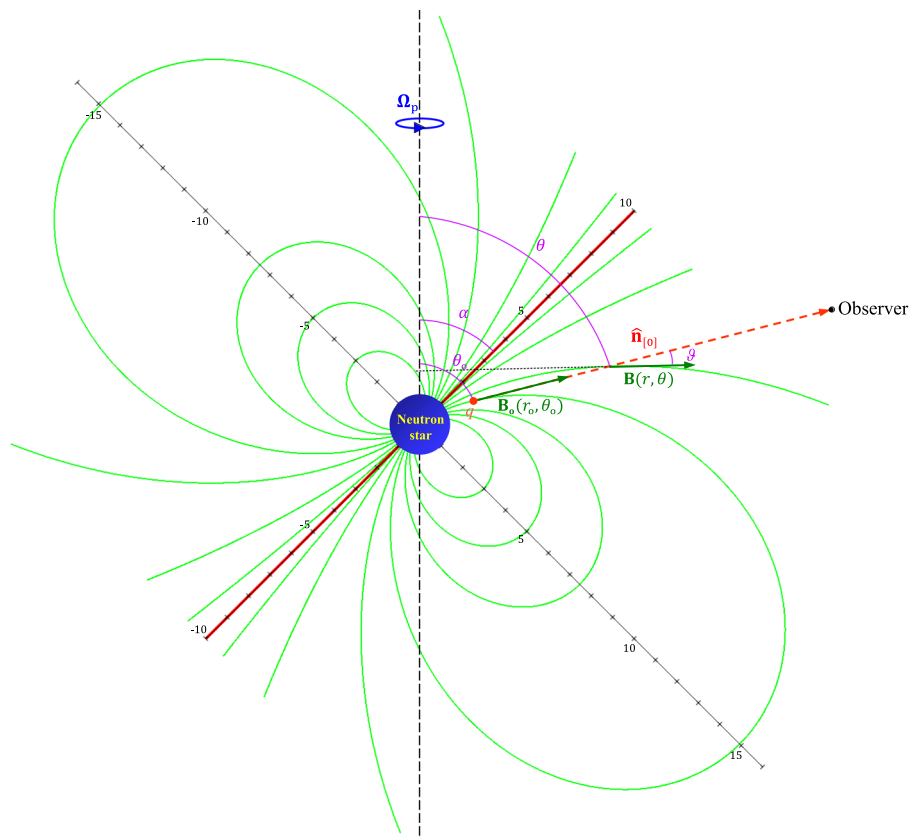
The paper is organized as follows. In Sect. 2.1, we introduce a system of evolution equations of the Stokes vector and apply this formalism to our pulsar emission model for an oblique dipole rotator. In Sect. 2.2, the evolution equations are solved for some known rotation-powered pulsars (RPPs) in three ways: fully numerically, via perturbation analysis, and using an analytical approximation. Also, we discuss the evolution patterns of the Stokes vectors resulting from the solutions. In Sect. 3.1, we consider a magnetic quadrupole model for pulsar emission and look into the evolution equations under this model. In Sect. 3.2, we solve the evolution equations for the same RPPs fully numerically, and compare the results with those for the dipole case in Sect. 2.2. Then finally, we conclude the paper with discussions on other similar studies and future follow-up studies.

2 Evolution of polarization states in strong magnetic field – dipole pulsars

2.1 Evolution equations of Stokes vector

Classically, polarization properties of pulsar emission are described by the Stokes parameters $\{I, Q, U, V\}$, where I is a measure of the total intensity, Q and U jointly describe the linear polarization, and V describes the circular polariza-

Fig. 1 A cross-sectional view of a pulsar magnetosphere with the dipole magnetic field lines (green) around a neutron star. The vertical dashed line (black) and the inclined solid line (red) represent the rotation axis and the magnetic axis, respectively. α between these axes denotes the inclination angle. The scale of the unity in this graph is equivalent to the neutron star radius $\sim 10^6$ cm. The red dashed line represents the trajectory curve of the light ray traced by the propagation vector $\hat{\mathbf{n}}_{[0]}$ as projected onto the xz -plane (Credit: [37], reproduced with modifications)



tion of pulsar emission (for more details, see Appendix A). However, in the presence of a strong magnetic field in the background of the emission, the polarization evolves along the photon propagation path from the emission point towards an observer. The evolution of the polarization can be investigated systematically using the formalism initiated by [31–33], and further developed by [29, 34–36], namely, a system of evolution equations of the Stokes vector, described as

$$\frac{d\mathbf{S}}{ds} = k\hat{\Omega} \times \mathbf{S}, \tag{1}$$

where $k \equiv \omega/c$ denotes the wave number for the electromagnetic radiation and s is an affine parameter to measure the length of the photon trajectory, and \mathbf{S} is the normalized Stokes vector, defined out of the Stokes parameters as $\mathbf{S} = (S_1, S_2, S_3) \equiv (Q/I, U/I, V/I)$,¹ and $\hat{\Omega}$ is the dimensionless birefringent vector, defined as²

$$\hat{\Omega} \equiv \frac{\alpha_e}{30\pi} (B/B_c)^2 \sin^2 \vartheta \left(\mathcal{E}_I^2 - \mathcal{E}_{II}^2, 2\mathcal{E}_I\mathcal{E}_{II}, 0 \right), \tag{2}$$

where α_e denotes the fine-structure constant and $\alpha_e/(30\pi) \approx 7.743 \times 10^{-5}$ and $B_c \approx 4.414 \times 10^{13}$ G is the critical magnetic

¹ The classical Stokes vector can be expressed via pulse profiles of pulsar curvature emission, as illustrated in Appendix A.

² Note that our $k\hat{\Omega}$ is equivalent to the birefringent vector as defined in the references above.

field, and ϑ denotes the angle between the photon trajectory and the local magnetic field line (see Fig. 1), i.e.,

$$\vartheta = \cos^{-1} \left(\hat{\mathbf{n}}_{[0]} \cdot \hat{\mathbf{B}} \right), \tag{3}$$

with $\hat{\mathbf{n}}_{[0]}$ being the classical propagation vector and $\hat{\mathbf{B}} \equiv \mathbf{B}/|\mathbf{B}|$, and

$$\mathcal{E}_i \equiv -\hat{\mathbf{B}} \cdot (\hat{\mathbf{n}}_{[0]} \times \mathbf{e}_{i[0]}), \quad i = \text{I, II}, \tag{4}$$

with $\mathbf{e}_{\text{I}[0]}$ and $\mathbf{e}_{\text{II}[0]}$ being the two classical mode polarization vectors, orthogonal to each other and to $\hat{\mathbf{n}}_{[0]}$; the specific forms of $\hat{\mathbf{n}}_{[0]}$, $\mathbf{e}_{\text{I}[0]}$ and $\mathbf{e}_{\text{II}[0]}$ are later given by Eqs. (8), (12) and (13), respectively, for the magnetic field of an oblique dipole rotator as described by Eq. (5) and Fig. 1.

In our pulsar emission model, we consider curvature radiation produced along the magnetic field lines of an oblique dipole rotator as illustrated in Fig. 1:

$$\begin{aligned} \mathbf{B}(r, \theta, \phi) = & \frac{2\mu (\cos \alpha \cos \theta + \sin \alpha \sin \theta \cos \phi)}{r^3} \mathbf{e}_r \\ & + \frac{\mu (\cos \alpha \sin \theta - \sin \alpha \cos \theta \cos \phi)}{r^3} \mathbf{e}_\theta \\ & + \frac{\mu \sin \alpha \sin \phi}{r^3} \mathbf{e}_\phi, \end{aligned} \tag{5}$$

where μ is the magnetic dipole moment and α denotes the inclination angle between the rotation axis and the mag-

netic axis.³ The photon beam from curvature radiation is tangent to the field line at the emission point $(x_o, y_o, z_o) = (r_o \sin \theta_o, 0, r_o \cos \theta_o)$.

However, at the same time, our pulsar magnetosphere rotates, and therefore the field lines get twisted due to the magneto-centrifugal acceleration on the plasma particles moving along the field lines [38]. Then, taking into consideration this magneto-hydrodynamic (MHD) effect, the direction of the classical photon propagation, which must line up with the particle velocity in order for an observer to receive the radiation, can be described as [39]

$$\hat{\mathbf{n}}_{[0]} = \beta \hat{\mathbf{B}} + \frac{\boldsymbol{\Omega}_p \times \mathbf{r}}{c}, \tag{6}$$

where on the right-hand side

$$\beta \equiv \left[1 - \left(\frac{\Omega_p r}{c} \right)^2 \sin^2 \theta \left(1 - \frac{\sin^2 \alpha \sin^2 \phi}{3 \cos^2 \theta' + 1} \right) \right]^{1/2} - \frac{\Omega_p r}{c} \frac{\sin \alpha \sin \theta \sin \phi}{(3 \cos^2 \theta' + 1)^{1/2}}, \tag{7}$$

with c being the speed of light and $\cos \theta' \equiv \cos \alpha \cos \theta + \sin \alpha \sin \theta \cos \phi$, and the second term accounts for the centrifugal acceleration, with $\boldsymbol{\Omega}_p \equiv \Omega_p \mathbf{e}_z$ ⁴ and $\Omega_p = 2\pi/P$ being a pulsar rotation (angular) frequency, as given in terms of the rotation period P .

During the rotation the azimuthal phase changes by $\phi \sim \Omega_p t$, while our photon has propagated a distance by $s \sim ct$. In our analysis, the photon propagation is described with the consideration of the MHD effect above, assuming ϕ to be very small; e.g., $\phi \lesssim 10^{-1}$ is considered for a millisecond pulsar with $\Omega_p \sim 10^2$ Hz, during the time of rotation $t \lesssim 10^{-3}$ s, such that $s \lesssim 10^7$ cm, which corresponds to the propagation distance within about 10 times the neutron star radius. For Eq. (6) we take only the leading order expansions of $\hat{\mathbf{B}}(r_o, \theta_o, \phi)$ and $\beta(r_o, \theta_o, \phi)$ in ϕ from Eqs. (5) and (7), respectively, and can express the classical propagation vector

$\hat{\mathbf{n}}_{[0]}$ in Cartesian coordinates as

$$\hat{\mathbf{n}}_{[0]} = \hat{n}_{x[0]} \mathbf{e}_x + \hat{n}_{y[0]} \mathbf{e}_y + \hat{n}_{z[0]} \mathbf{e}_z \tag{8}$$

with

$$\hat{n}_{x[0]} \approx \frac{2 \cos(\theta_o - \alpha) \sin \theta_o + \sin(\theta_o - \alpha) \cos \theta_o}{(3 \cos^2(\theta_o - \alpha) + 1)^{1/2}} + \mathcal{O}\left(\phi^2, (\Omega_p r_o/c)^2, \phi (\Omega_p r_o/c)\right), \tag{9}$$

$$\hat{n}_{z[0]} \approx \frac{2 \cos(\theta_o - \alpha) \cos \theta_o - \sin(\theta_o - \alpha) \sin \theta_o}{(3 \cos^2(\theta_o - \alpha) + 1)^{1/2}} + \mathcal{O}\left(\phi^2, (\Omega_p r_o/c)^2, \phi (\Omega_p r_o/c)\right), \tag{10}$$

and

$$\hat{n}_{y[0]} \approx \frac{\Omega_p}{c} \left[\frac{\sin \alpha s}{(3 \cos^2(\theta_o - \alpha) + 1)^{1/2}} + r_o \sin \theta_o \right] + \mathcal{O}\left(\phi^2, (\Omega_p r_o/c)^2, \phi (\Omega_p r_o/c)\right), \tag{11}$$

where we have considered $\Omega_p r_o/c \lesssim \phi$, e.g., for a millisecond pulsar with $\Omega_p \sim 10^2$ Hz and $r_o \sim 10^6$ cm, such that $(\Omega_p r_o/c)^2 \lesssim \phi (\Omega_p r_o/c) \lesssim \phi^2$, all to be ignored in our analysis, and have substituted $\phi = \Omega_p s/c$ in Eq. (11), the leading order rotational effect to be considered in our analysis.

The orthogonal pair of classical mode polarization vectors, $\boldsymbol{\epsilon}_{\text{I}[0]}$ and $\boldsymbol{\epsilon}_{\text{II}[0]}$, both being also orthogonal to $\hat{\mathbf{n}}_{[0]}$ as given by Eq. (8) above, are determined as

$$\boldsymbol{\epsilon}_{\text{I}[0]} = \hat{n}_{z[0]} \mathbf{e}_x + \hat{n}_{y[0]} \mathbf{e}_y - \hat{n}_{x[0]} \mathbf{e}_z, \tag{12}$$

$$\boldsymbol{\epsilon}_{\text{II}[0]} = -(\hat{n}_{x[0]} + \hat{n}_{z[0]}) \hat{n}_{y[0]} \mathbf{e}_x + \mathbf{e}_y + (\hat{n}_{x[0]} - \hat{n}_{z[0]}) \hat{n}_{y[0]} \mathbf{e}_z, \tag{13}$$

such that the three vectors, $\hat{\mathbf{n}}_{[0]}$, $\boldsymbol{\epsilon}_{\text{I}[0]}$ and $\boldsymbol{\epsilon}_{\text{II}[0]}$ form an orthonormal basis.⁵ Using these for Eq. (4), we obtain

$$\begin{aligned} \mathcal{E}_{\text{I}} = -\hat{\mathbf{B}} \cdot (\hat{\mathbf{n}}_{[0]} \times \boldsymbol{\epsilon}_{\text{I}[0]}) &\approx \frac{4 \cos(\theta_o - \alpha) \cos(\theta - \alpha) + \sin(\theta_o - \alpha) \sin(\theta - \alpha) + 2 \sin(\theta - \theta_o)}{(3 \cos^2(\theta_o - \alpha) + 1)^{1/2} (3 \cos^2(\theta - \alpha) + 1)^{1/2}} \hat{n}_{y[0]} \\ &- \frac{\Omega_p \sin \alpha s}{c (3 \cos^2(\theta - \alpha) + 1)^{1/2}} + \mathcal{O}\left(\phi^2, (\Omega_p r_o/c)^2, \phi (\Omega_p r_o/c)\right), \end{aligned} \tag{14}$$

$$\mathcal{E}_{\text{II}} = -\hat{\mathbf{B}} \cdot (\hat{\mathbf{n}}_{[0]} \times \boldsymbol{\epsilon}_{\text{II}[0]}) \approx -\frac{2 \sin(\theta - \theta_o)}{(3 \cos^2(\theta_o - \alpha) + 1)^{1/2} (3 \cos^2(\theta - \alpha) + 1)^{1/2}} + \mathcal{O}\left(\phi^2, (\Omega_p r_o/c)^2, \phi (\Omega_p r_o/c)\right). \tag{15}$$

³ Here the symbol α must be distinguished from the fine-structure constant α_e .

⁴ Here the symbol $\boldsymbol{\Omega}_p$ must be distinguished from the birefringent vector $\hat{\boldsymbol{\Omega}}$.

⁵ It can be checked out that $\hat{\mathbf{n}}_{[0]} \cdot \boldsymbol{\epsilon}_{\text{I}[0]} \approx 0 + \mathcal{O}\left((\Omega_p r_o/c)^2\right)$, $\hat{\mathbf{n}}_{[0]} \cdot \boldsymbol{\epsilon}_{\text{II}[0]} = 0$ and $\boldsymbol{\epsilon}_{\text{I}[0]} \cdot \boldsymbol{\epsilon}_{\text{II}[0]} = 0$ while $\hat{\mathbf{n}}_{[0]}^2 \approx 1 + \mathcal{O}\left((\Omega_p r_o/c)^2\right)$ and $\boldsymbol{\epsilon}_{\text{I,II}[0]}^2 \approx 1 + \mathcal{O}\left((\Omega_p r_o/c)^2\right)$.

By means of Eqs. (3), (5) and (8) one can express

$$\cos \vartheta \approx \frac{4 \cos(\theta_0 - \alpha) \cos(\theta - \alpha) + \sin(\theta_0 - \alpha) \sin(\theta - \alpha)}{(3 \cos^2(\theta_0 - \alpha) + 1)^{1/2} (3 \cos^2(\theta - \alpha) + 1)^{1/2}} + \mathcal{O}\left(\phi^2, (\Omega_p r_o/c)^2, \phi(\Omega_p r_o/c)\right), \tag{16}$$

$$\sin \vartheta \approx \frac{2 \sin(\theta - \theta_0)}{(3 \cos^2(\theta_0 - \alpha) + 1)^{1/2} (3 \cos^2(\theta - \alpha) + 1)^{1/2}} + \mathcal{O}\left(\phi^2, (\Omega_p r_o/c)^2, \phi(\Omega_p r_o/c)\right). \tag{17}$$

Now, using the relations between Eqs. (14)–(17), the birefringent vector can finally be specified from Eq. (2):

$$\hat{\Omega}_1 \approx -\eta B^2 \sin^4 \vartheta + \mathcal{O}\left(\phi^2, (\Omega_p r_o/c)^2, \phi(\Omega_p r_o/c)\right), \tag{18}$$

$$\hat{\Omega}_2 \approx -2\eta B^2 \sin^3 \vartheta \left[(\cos \vartheta + \sin \vartheta) \hat{n}_{y[0]} - \frac{\Omega_p \sin \alpha s}{c (3 \cos^2(\theta - \alpha) + 1)^{1/2}} \right] + \mathcal{O}\left(\phi^2, (\Omega_p r_o/c)^2, \phi(\Omega_p r_o/c)\right), \tag{19}$$

where $\eta \equiv \alpha_e / (30\pi B_c^6)$ and

$$B = \frac{B_{\max} r_*^3 (3 \cos^2(\theta - \alpha) + 1)^{1/2}}{2(x^2 + z^2)^{3/2}}, \tag{20}$$

with B_{\max} being the maximum magnetic field intensity at the polar cap⁷ and r_* being the neutron star radius ($\approx 10^6$ cm), and $\hat{n}_{y[0]}$, $\cos \vartheta$ and $\sin \vartheta$ are given by Eqs. (11), (16) and (17), respectively.

To facilitate solving the evolution equation (1) in the next subsection, we substitute the following identities,

$$\begin{aligned} \cos(\theta - \alpha) &= \frac{\sin \alpha x + \cos \alpha z}{(x^2 + z^2)^{1/2}}, \\ \sin(\theta - \alpha) &= \frac{\cos \alpha x - \sin \alpha z}{(x^2 + z^2)^{1/2}}, \\ \sin(\theta - \theta_0) &= \frac{\cos \theta_0 x - \sin \theta_0 z}{(x^2 + z^2)^{1/2}}, \end{aligned} \tag{21}$$

together with

$$x = \hat{n}_{x[0]}s + r_o \sin \theta_0, \quad z = \hat{n}_{z[0]}s + r_o \cos \theta_0 \tag{22}$$

⁶ $\eta = \eta_2 - \eta_1$, where η_1 and η_2 are parameters defined via $\eta_1/4 = \eta_2/7 = \alpha_e / (90\pi B_c^2) \sim 10^{-31} \text{ g}^{-1} \text{ cm s}^2$, from the post-Maxwellian Lagrangian $\mathcal{L}_{\text{PM}} = -(\mathbf{B}^2 - \mathbf{E}^2)/2 + \eta_1(\mathbf{B}^2 - \mathbf{E}^2)^2/4 + \eta_2(\mathbf{E} \cdot \mathbf{B})^2$ [40].

⁷ From Eq. (5) $B_{\max} = |B(r = r_*, \theta = \alpha)|$.

into (16) and (17). Then our solutions for the Stokes vector \mathbf{S} will be parameterized solely by s .

2.2 Solving the evolution equations

From Eq. (1) we write down a system of first-order ordinary differential equations to solve:

$$\dot{S}_1(s) = k \hat{\Omega}_2(s) S_3(s), \tag{23}$$

$$\dot{S}_2(s) = -k \hat{\Omega}_1(s) S_3(s), \tag{24}$$

$$\dot{S}_3(s) = k \left[\hat{\Omega}_1(s) S_2(s) - \hat{\Omega}_2(s) S_1(s) \right], \tag{25}$$

where an over-dot $\dot{}$ denotes differentiation with respect to s , and $\hat{\Omega}_1(s)$ and $\hat{\Omega}_2(s)$ are given by (18) and (19), respectively. By solving these equations numerically, we find out how the photon polarization evolves through the strong magnetic field in the background of our pulsar emission.

However, in case $|k \hat{\Omega}_{1,2}(s) s|_{\max} \ll 1$, one can obtain a solution to Eq. (1) via perturbation:

$$\mathbf{S} = \mathbf{S}_{[0]} + \delta \mathbf{S}_{[1]} = \mathbf{S}_{[0]} + k \int \hat{\boldsymbol{\Omega}} \times \mathbf{S}_{[0]} ds, \tag{26}$$

where $\delta \mathbf{S}_{[1]}$ means the leading order quantum correction to the unperturbed (initial) Stokes vector $\mathbf{S}_{[0]}$. Here the correction can be treated as the leading order perturbation with $\alpha_e / (30\pi) (B/B_c)^2 \sim 10^{-5} (B/B_c)^2$ being a perturbation parameter. Upon inspection of Eqs. (18) and (19) for Eq. (26), we can further write down our solution in terms of its components:

$$S_1 \approx S_{1[0]} - 2k\eta S_{3[0]} \int B^2 \sin^3 \vartheta \left[(\cos \vartheta + \sin \vartheta) \hat{n}_{y[0]} - \frac{\Omega_p \sin \alpha s}{c (3 \cos^2(\theta - \alpha) + 1)^{1/2}} \right] ds, \tag{27}$$

$$S_2 \approx S_{2[0]} + k\eta S_{3[0]} \int B^2 \sin^4 \vartheta ds, \tag{28}$$

$$S_3 \approx S_{3[0]} + k\eta \left\{ 2S_{1[0]} \int B^2 \sin^3 \vartheta \left[(\cos \vartheta + \sin \vartheta) \hat{n}_{y[0]} - \frac{\Omega_p \sin \alpha s}{c (3 \cos^2(\theta - \alpha) + 1)^{1/2}} \right] ds - S_{2[0]} \int B^2 \sin^4 \vartheta ds \right\}. \tag{29}$$

2.2.1 Examples

We consider X-ray emissions from three neutron stars: (i) one with $B_{\max} \approx 10^{12}$ G and $\Omega_p \approx 392.7$ Hz ($P \approx 0.016$ s), (ii) another with $B_{\max} \approx 5.6 \times 10^{12}$ G and $\Omega_p \approx 22.28$ Hz ($P \approx 0.282$ s), (iii) the third with $B_{\max} \approx 5.0 \times 10^{13}$ G and $\Omega_p \approx 19.6$ Hz ($P \approx 0.32$ s). For all three, we assume $r_o = 2r_* \approx 2 \times 10^6$ cm, $\theta_0 = 60^\circ$, $\alpha = 45^\circ$, $\eta \approx 3.97 \times 10^{-32}$ and

$\omega \approx 2\pi \times 10^{18}$ Hz ($k \approx 2.0958 \times 10^8$ cm⁻¹).⁸ These stars belong to ‘rotation-powered pulsars’ (RPPs) [41].⁹ In Fig. 2 the three RPPs chosen from the X-ray group are encircled: (i) the one in orange, (ii) another in cyan, (iii) the third in green. Given the X-ray emissions from these, we solve the evolution equations (1) for the following cases.

Example (i)

With $B_{\max} \approx 10^{12}$ G and $\Omega_p \approx 392.7$ Hz ($P \approx 0.016$ s), we obtain numerical solutions of Eqs. (23)–(25) (in solid lines) or perturbative solutions by means of Eqs. (27)–(29) (in dashed lines), as shown in Fig. 3a, b, given the initial Stokes vectors $\mathbf{S}(0) = (S_1(0), S_2(0), S_3(0)) = (1, 0, 0)$ and $(0.8, 0, 0.6)$, respectively. The perturbative solutions agree well with numerical ones as $|k\hat{\Omega}_{1,2}(s)s|_{\max} \sim |k\hat{\Omega}_{1,2}(s_{\pm 1,2})s_{\pm 1,2}| \sim 10^{-2} \ll 1$, where $s_{\pm 1,2}$ is the extremum, i.e., $d\hat{\Omega}_{1,2}(s_{\pm 1,2})/ds = 0$. On the Poincaré sphere, our solutions are represented by the magenta and light blue loci in Fig. 6a, corresponding to Fig. 3a, b, respectively. The loci imply a fraction of an oscillation for the polarization evolution, as is confirmed later by the approximate analytical solutions in Sect. 2.2.2.

Example (ii)

With $B_{\max} \approx 5.6 \times 10^{12}$ G and $\Omega_p \approx 22.28$ Hz ($P \approx 0.282$ s), we obtain numerical solutions of Eqs. (23)–(25), as shown in Fig. 4a, b, given the initial Stokes vectors $\mathbf{S}(0) = (S_1(0), S_2(0), S_3(0)) = (1, 0, 0)$ and $(0.8, 0, 0.6)$, respectively. On the Poincaré sphere, our solutions are represented by the magenta and light blue loci in Fig. 6b, corresponding to Fig. 4a, b, respectively. The loci imply about half an oscillation for the polarization evolution, as is confirmed later by the approximate analytical solutions in Sect. 2.2.2.

Example (iii)

With $B_{\max} \approx 5.0 \times 10^{13}$ G and $\Omega_p \approx 19.6$ Hz ($P \approx 0.32$ s), we obtain numerical solutions of Eqs. (23)–(25), as shown in Fig. 5a, b, given the initial Stokes vectors $\mathbf{S}(0) = (S_1(0), S_2(0), S_3(0)) = (1, 0, 0)$ and $(0.8, 0, 0.6)$, respectively. On the Poincaré sphere, our solutions are represented by the magenta and light blue loci in Fig. 6c, corresponding to Fig. 5a, b, respectively. The loci imply multiple oscillations for the polarization evolution, as is confirmed later by the approximate analytical solutions in Sect. 2.2.2.

With regard to the adiabatic evolution condition as mentioned in Refs. [29,34,35], we carefully examine our results presented in Figs. 3, 4 and 5 to see what interpretations the condition leads to. Solving the condition $|k\hat{\Omega} (d \ln |k\hat{\Omega}|/ds)^{-1}| \gtrsim 0.05$ for s yields $s_{\text{PL1}} \lesssim s \lesssim s_{\text{PL2}}$,¹⁰ where $s_{\text{PL1[2]}}$ refers to the lower [upper] bound for the ‘polarization limiting’ distance as measured from the emission point. Using this, one can check out the following: (1) for 6.2×10^5 cm $\lesssim s \lesssim 1.8 \times 10^6$ cm in Fig. 3, (2) for 3.1×10^5 cm $\lesssim s \lesssim 6.2 \times 10^6$ cm in Fig. 4, (3) for 1.1×10^5 cm $\lesssim s \lesssim 1.9 \times 10^7$ cm in Fig. 5, our Stokes vector evolves evidently; otherwise, it freezes.

2.2.2 Approximate analytical solutions

Plotting the birefringent functions $\hat{\Omega}_1(s)$ and $\hat{\Omega}_2(s)$, as given by (18) and (19), respectively, one can observe that they feature distinctive patterns; they can be well approximated by some analytic models, whose curves resemble the original plots. In Fig. 7 are plotted the birefringent functions for the three cases: (a) $B_{\max} \approx 10^{12}$ G and $\Omega_p \approx 392.7$ Hz ($P \approx 0.016$ s), (b) $B_{\max} \approx 5.6 \times 10^{12}$ G and $\Omega_p \approx 22.28$ Hz ($P \approx 0.282$ s), (c) $B_{\max} \approx 5.0 \times 10^{13}$ G and $\Omega_p \approx 19.6$ Hz ($P \approx 0.32$ s) with solid lines (see Fig. 7a–c, respectively), where they have been evaluated with the same initial condition as assumed in Sect. 2.2.1.

In correspondence with the actual birefringent functions above, the following analytical models are also plotted with dashed lines in Fig. 7:

$$\hat{\Omega}_{1,2}(s) \approx -a_{1,2}s^{\frac{p+1}{p}}e^{-bs} \text{ for } 0 \leq s \leq 20r_* (\approx 2 \times 10^7 \text{ cm}), \tag{30}$$

where $a_1 > 0, a_2 < 0, b > 0$ and $p > 0$ are free parameters; with suitable values chosen for these, our model functions can give rise to solutions of Eqs. (23)–(25) that match fairly well the numerical results obtained in Sect. 2.2.1. Here we express

$$a_{1,2} = -\hat{\Omega}_{1(\min),2(\max)} \left[\frac{e}{(1-q)s_{\pm 1} + qs_{\pm 2}} \right]^{\frac{p+1}{p}}, \tag{31}$$

$$b = \frac{p+1}{p[(1-q)s_{\pm 1} + qs_{\pm 2}]},$$

where $\hat{\Omega}_{1(\min),2(\max)} = \hat{\Omega}_{1,2}(s_{\pm 1,2})$, evaluated from (18), (19), with $s_{\pm 1,2}$ denoting the extremum. We have set $p = 100$

⁸ For the emission location (r_e, θ_e) and the inclination angle α are given the same values for the three stars; the values are not based on actual observations. This is intended for comparing the QED effects from the three different sources under the same conditions.

⁹ RPPs refer to neutron stars whose radiation is powered by loss of their rotation energy, via creation and acceleration of e^+e^- pairs in the strong magnetic field, $B_{\max} \sim 10^{11} - 10^{13}$ G. The number of detected RPPs are known to be about ~ 4000 in radio, ~ 10 in optical (including NIR and UV), ~ 100 in X-ray and ~ 300 in gamma-ray emissions [41–43].

¹⁰ Note that our $k\hat{\Omega}$ is equivalent to the birefringent vector as defined in Refs. [29,34,35] and that we set the condition value to 0.05 rather than 0.5 as in the references.

Fig. 2 The population of detected rotation-powered pulsars (RPPs) plotted against their rotation period. RPPs detected in X-rays and gamma-rays are represented by red dots and blue stars, respectively. Three RPPs chosen from the X-ray group, (i) one with $B_{\max} \approx 10^{12}$ G and $\Omega_p \approx 392.7$ Hz ($P \approx 0.016$ s), (ii) another with $B_{\max} \approx 5.6 \times 10^{12}$ G and $\Omega_p \approx 22.28$ Hz ($P \approx 0.282$ s), (iii) the third with $B_{\max} \approx 5.0 \times 10^{13}$ G and $\Omega_p \approx 19.6$ Hz ($P \approx 0.32$ s), are encircled in orange, cyan and green colors, respectively (Credit: [41], reproduced with modifications)

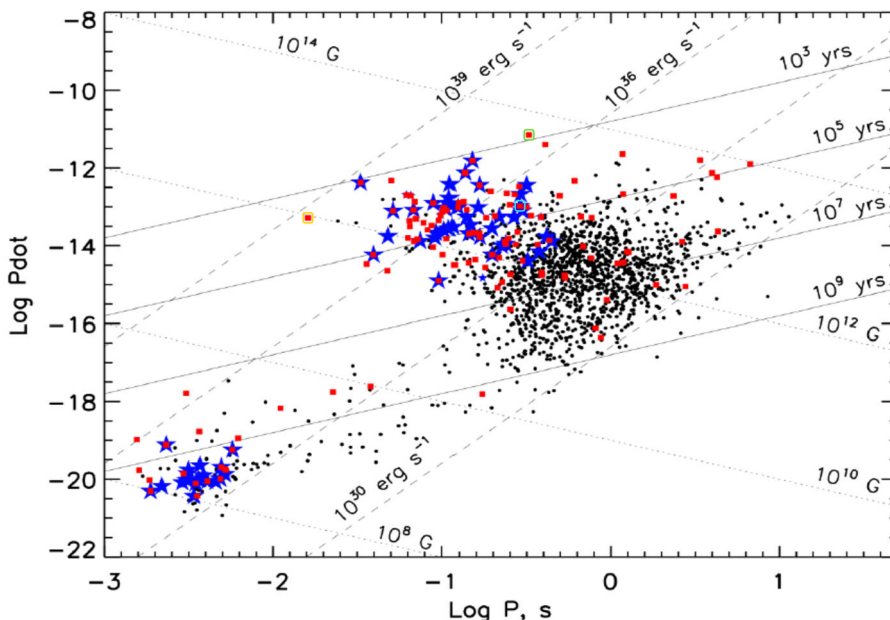
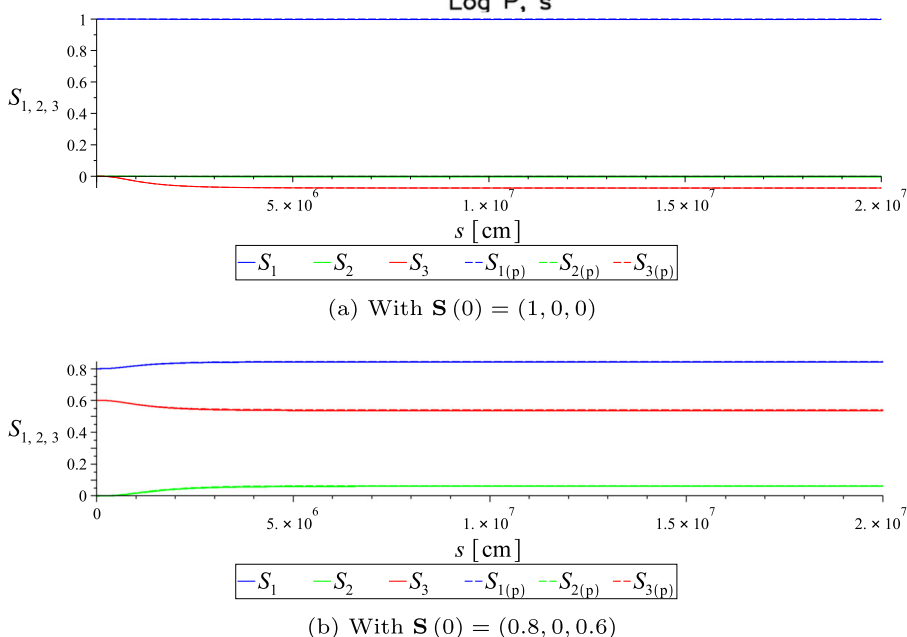


Fig. 3 For Example (i): the evolution of the Stokes vector $\mathbf{S}(s) = (S_1(s), S_2(s), S_3(s))$, $0 \leq s \leq 20r_*$ ($\approx 2 \times 10^7$ cm), for the X-ray emissions from the pulsar with $B_{\max} \approx 10^{12}$ G and $\Omega_p \approx 392.7$ Hz ($P \approx 0.016$ s); the subscript (p) stands for ‘perturbative’



(a sufficiently large number) for all three cases, and $q = 0.99999$ for (a) and (b), and $q = 0.0532$ for (c) in Fig. 7,¹¹

Plugging Eq. (30) into Eqs. (23)–(25), we obtain analytical solutions as follows (for a complete derivation, see Appendix B):

$$S_1(s) \approx \frac{a_2 S_0}{\sqrt{a_1^2 + a_2^2}} \cos(\Psi(s; p) + \delta) + \frac{a_1 C}{\sqrt{a_1^2 + a_2^2}}, \quad (32)$$

$$S_2(s) \approx -\frac{a_1 S_0}{\sqrt{a_1^2 + a_2^2}} \cos(\Psi(s; p) + \delta) + \frac{a_2 C}{\sqrt{a_1^2 + a_2^2}}, \quad (33)$$

¹¹ In particular, the values for q have been chosen such that our solutions converge to the asymptotic limits that match well the numerical results given by Figs. 3b, 4b and 5b in Sect. 2.2.1, as s tends to ∞ .

$$S_3(s) \approx S_0 \sin(\Psi(s; p) + \delta), \quad (34)$$

where

$$\Psi(s; p) \equiv k \sqrt{a_1^2 + a_2^2} b^{-\frac{4p+1}{2p}} s^{\frac{1}{2p}} e^{-\frac{1}{2}bs} \times \left[M_{\frac{1}{2p}, \frac{p+1}{2p}}(bs) - (bs)^{\frac{2p+1}{2p}} e^{-\frac{1}{2}bs} \right], \quad (35)$$

and $M_{\kappa, \mu}(z)$ denotes a Whittaker function of the first kind,¹² and $a_{1,2}$ and b are given by (31). Here we determine S_0, C and

¹² The expression inside the square brackets in Eq. (35) has been reduced from its original form as given by Eq. (B7) in Appendix B, using the identity $M_{(2p+1)/(2p), (p+1)/(2p)}(bs) = (bs)^{(2p+1)/(2p)} e^{-bs/2} M(0, (2p+1)/p, bs)$, with the Kummer function $M(0, (2p+1)/p, bs) = 1$ as a special case [44].

Fig. 4 For Example (ii): the evolution of the Stokes vector $\mathbf{S}(s) = (S_1(s), S_2(s), S_3(s))$, $0 \leq s \leq 20r_*$ ($\approx 2 \times 10^7$ cm), for the X-ray emissions from the pulsar with $B_{\max} \approx 5.6 \times 10^{12}$ G and $\Omega_p \approx 22.28$ Hz ($P \approx 0.282$ s)

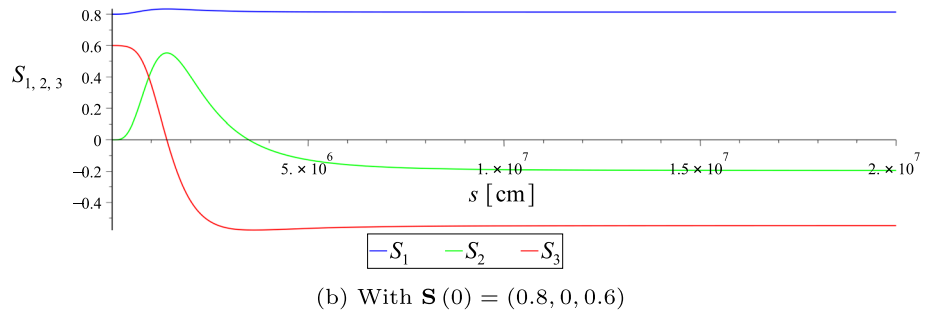
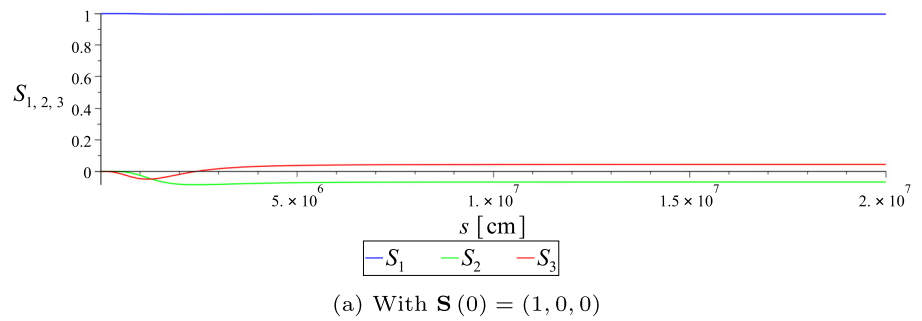


Fig. 5 For Example (iii): the evolution of the Stokes vector $\mathbf{S}(s) = (S_1(s), S_2(s), S_3(s))$, $0 \leq s \leq 20r_*$ ($\approx 2 \times 10^7$ cm), for the X-ray emissions from the pulsar with $B_{\max} \approx 5.0 \times 10^{13}$ G and $\Omega_p \approx 19.6$ Hz ($P \approx 0.32$ s)

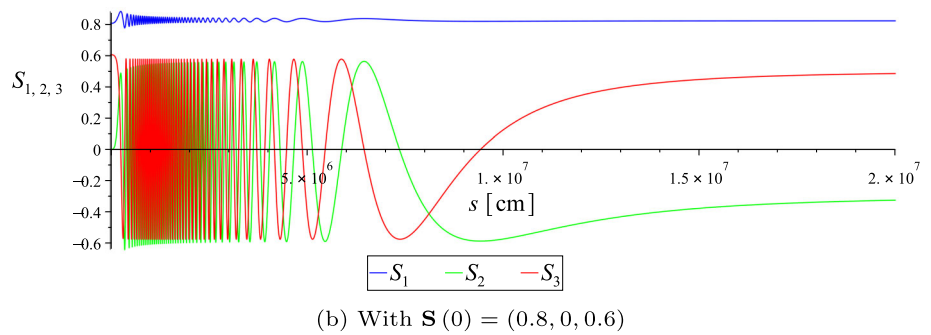
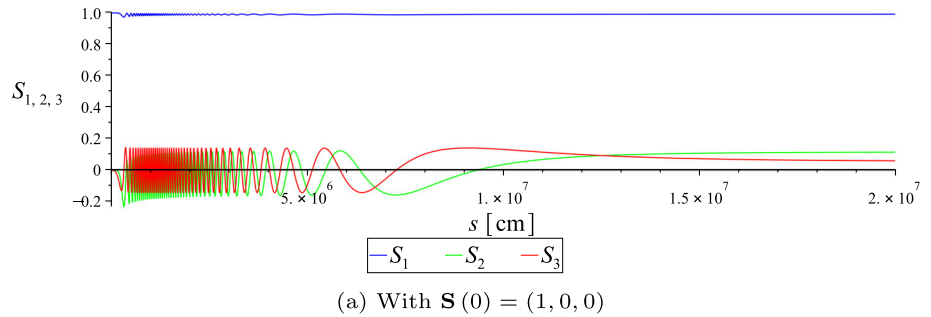


Fig. 6 Representations of the Stokes vectors from Examples (i)–(iii) on the Poincaré sphere. The loci imply patterns of the polarization evolution in terms of oscillation

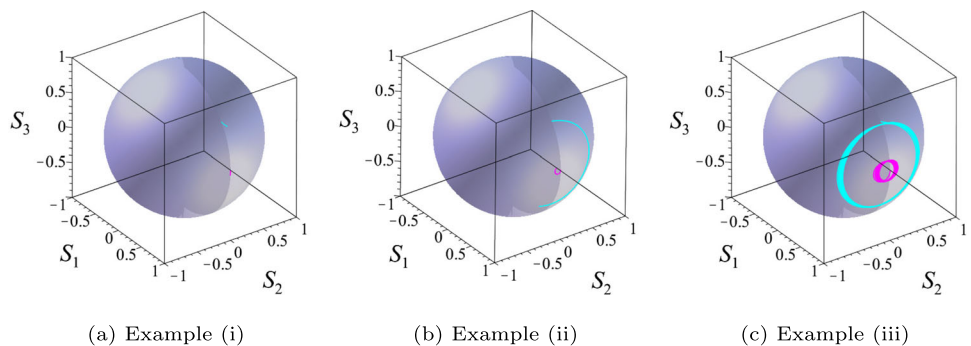
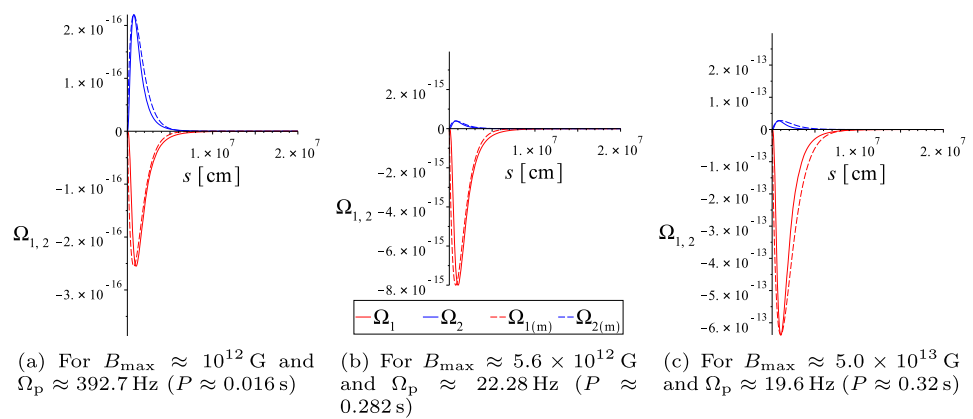


Fig. 7 Plots of the birefringent functions $\hat{\Omega}_1(s)$ and $\hat{\Omega}_2(s)$ and their approximate analytic models $\hat{\Omega}_{1(m)}(s)$ and $\hat{\Omega}_{2(m)}(s)$



δ by matching the initial value of the Stokes vector $\mathbf{S}(0) = (S_1(0), S_2(0), S_3(0))$ with Eqs. (32)–(34) evaluated at $s = 0$.

In Fig. 8 we plot the above solutions (32)–(34) for the following cases, assuming $r_o = 2r_* \approx 2 \times 10^6$ cm, $\theta_o = 60^\circ$, $\alpha = 45^\circ$, $\eta \approx 3.97 \times 10^{-32}$ for $\hat{\Omega}_{1(\min),2(\max)} = \hat{\Omega}_{1,2}(s_{\dagger 1,2})$ (evaluated via (18) and (19)) and $\omega \approx 2\pi \times 10^{18}$ Hz ($k \approx 2.0958 \times 10^8$ cm $^{-1}$) for the X-ray emissions, with the initial Stokes vector $\mathbf{S}(0) = (0.8, 0, 0.6)$:

Case (a) (see Fig. 8a); for $B_{\max} \approx 10^{12}$ G and $\Omega_p \approx 392.7$ Hz ($P \approx 0.016$ s), with the parameters $\hat{\Omega}_{1(\min)} \approx -2.5511 \times 10^{-16}$, $\hat{\Omega}_{2(\max)} \approx 2.2054 \times 10^{-16}$, $s_{\dagger 1} \approx 1.0202 \times 10^6$ cm, $s_{\dagger 2} \approx 7.5467 \times 10^5$ cm, $p = 100$, $q = 0.99999$ for $a_{1,2}$ and b (evaluated via (31)), and $S_o \approx 0.7961$, $C \approx 0.6052$, $\delta \approx 2.2879$,

Case (b) (see Fig. 8b); for $B_{\max} \approx 5.6 \times 10^{12}$ G and $\Omega_p \approx 22.28$ Hz ($P \approx 0.282$ s), with the parameters $\hat{\Omega}_{1(\min)} \approx -8.0001 \times 10^{-15}$, $\hat{\Omega}_{2(\max)} \approx 3.9240 \times 10^{-16}$, $s_{\dagger 1} \approx 1.0202 \times 10^6$ cm, $s_{\dagger 2} \approx 7.5467 \times 10^5$ cm, $p = 100$, $q = 0.99999$ for $a_{1,2}$ and b (evaluated via (31)), and $S_o \approx 0.6013$, $C \approx 0.7990$, $\delta \approx 1.6360$,

Case (c) (see Fig. 8c); for $B_{\max} \approx 5.0 \times 10^{13}$ G and $\Omega_p \approx 19.6$ Hz ($P \approx 0.32$ s), with the parameters $\hat{\Omega}_{1(\min)} \approx -6.3776 \times 10^{-13}$, $\hat{\Omega}_{2(\max)} \approx 2.7567 \times 10^{-14}$, $s_{\dagger 1} \approx 1.0202 \times 10^6$ cm, $s_{\dagger 2} \approx 7.5467 \times 10^5$ cm, $p = 100$, $q = 0.0532$ for $a_{1,2}$ and b (evaluated via (31)), and $S_o \approx 0.6010$, $C \approx 0.7993$, $\delta \approx 1.6283$.

These plots compare with Figs. 3b (for Example (i)), 4b (for Example (ii)) and 5b (for Example (iii)) in Sect. 2.2.1, respectively.

The analytical solutions (32)–(34) provide a useful tool for understanding the different patterns of polarization evolution for the three cases above, as given by Fig. 8a–c. Inspecting numerically the functional argument $\Psi(s; p)$ given by (35), one can approximate it to a simpler form with the help of (30) and (31):

For $0 \leq s \lesssim 2.5 \times 10^6$ cm,

$$\Psi(s; p = 100) = k\sqrt{a_1^2 + a_2^2}b^{-\frac{401}{200}}s^{\frac{1}{200}}e^{-\frac{1}{2}bs} \times \left[M_{\frac{1}{200}, \frac{101}{200}}(bs) - (bs)^{\frac{201}{200}}e^{-\frac{1}{2}bs} \right] \approx 0.24k\sqrt{\hat{\Omega}_{1(\min)}^2 + \hat{\Omega}_{2(\max)}^2}\pi s. \tag{36}$$

Using this, we can estimate how much the oscillations for the three cases have progressed, for example, during $0 \leq s \lesssim 2.5 \times 10^6$ cm:

$$\Psi\left(s \approx 2.5 \times 10^6 \text{ cm}; p = 100\right) \approx \begin{cases} 0.04\pi & \text{(a fraction of an oscillation) for Case (a),} \\ \pi & \text{(about half an oscillation) for Case (b),} \\ 80\pi & \text{(multiple oscillations) for Case (c),} \end{cases} \tag{37}$$

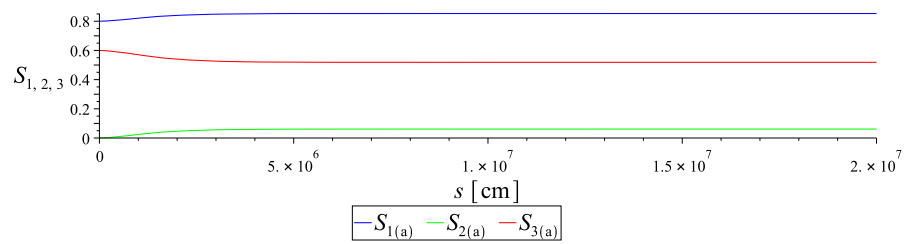
each of which can be checked by comparison with Fig. 8a–c, respectively.

Recalling Example (i) from Sect. 2.2.1, one finds that the condition for perturbation can be equivalently expressed with the help of (36):

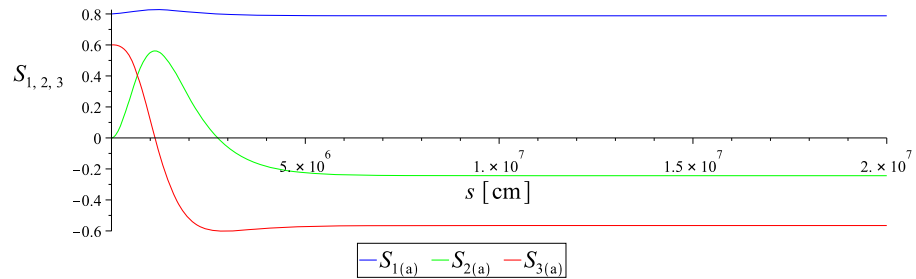
$$\left| k\hat{\Omega}_{1,2}(s) \right|_{\max} \sim \left| k\hat{\Omega}_{1,2}(s_{\dagger 1,2})s_{\dagger 1,2} \right| \sim 0.24k\sqrt{\hat{\Omega}_{1(\min)}^2 + \hat{\Omega}_{2(\max)}^2}\pi \times 10^6 \text{ cm} \approx 0.017\pi \ll 1 \text{ for Example (i) or Case (a).} \tag{38}$$

Extending this argument, similarly to (37) above we may state the following in reference to the patterns of polarization evolution:

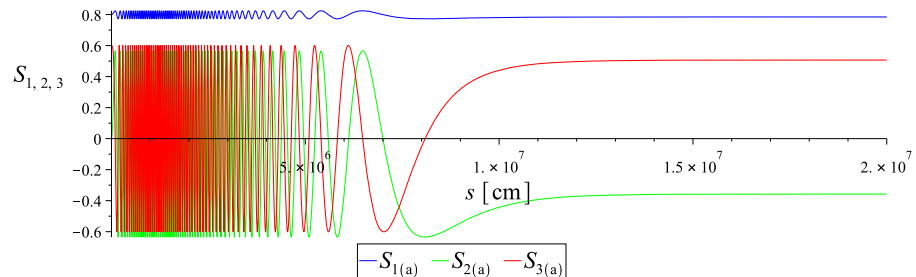
Fig. 8 Plots of the analytical solutions $S_{(a)}(s) = (S_{1(a)}(s), S_{2(a)}(s), S_{3(a)}(s))$, given the initial Stokes vector $S(0) = (0.8, 0, 0.6)$



(a) For $B_{\max} \approx 10^{12}$ G and $\Omega_p \approx 392.7$ Hz ($P \approx 0.016$ s)



(b) For $B_{\max} \approx 5.6 \times 10^{12}$ G and $\Omega_p \approx 22.28$ Hz ($P \approx 0.282$ s)



(c) For $B_{\max} \approx 5.0 \times 10^{13}$ G and $\Omega_p \approx 19.6$ Hz ($P \approx 0.32$ s)

$$|k\hat{\Omega}_{1,2}(s)s|_{\max} \begin{cases} \ll 1 & \text{(fractionally oscillatory - monotonic)} \\ \sim 1 & \text{(half oscillatory)} \\ \gg 1 & \text{(highly oscillatory)} \end{cases} \begin{matrix} \text{for Example (i),} \\ \text{for Example (ii),} \\ \text{for Example (iii).} \end{matrix} \quad (39)$$

These features can also be checked by comparison with the loci on the Poincaré sphere, as given by Fig. 6a–c, which imply the three different patterns of the polarization evolution in terms of oscillation (by means of the number of turns of the circular loci).

Here the approximate analytical solutions serve our purpose well, in that they help us to understand the different patterns of polarization evolution, which depend largely on the major profiles of pulsar emission, such as the emission frequency, the magnetic field strength and the rotation frequency of the neutron stars, as implied from Eq. (36). On the other hand, it would be worthwhile to check how close the numerical and analytical solutions are to each other by

evaluating the cross-correlations between them. For example, comparing Figs. 5b and 8c, over the entire region of polarization evolution ($2 \times 10^2 \text{ cm} \lesssim s \lesssim 2 \times 10^7 \text{ cm}$), the cross-correlation coefficients between S_1 and $S_{1(a)}$, between S_2 and $S_{2(a)}$, and between S_3 and $S_{3(a)}$ turn out to be approximately 0.9998, 0.6757, and 0.6521, respectively. This shows that the two solutions are in decent agreement with each other; although the asymptotic values, $S_1(\infty)$ and $S_{1(a)}(\infty)$, $S_2(\infty)$ and $S_{2(a)}(\infty)$, and $S_3(\infty)$ and $S_{3(a)}(\infty)$ are fairly closely matched to each other with less than 10% differences, the correlations are decreased by the mismatched phases between the two solutions.

3 Evolution of polarization states in strong magnetic field – quadrupole pulsars

3.1 Modified magnetic field geometry and evolution equations of Stokes vector

The pulsar magnetic field structure may not be assumed to be purely dipolar as given by (5). This assumption is based on the behavior of the field in the far-field regime, where its high-order multipole (ℓ) components decrease faster than low-order ones, like $r^{-(\ell+1)}$, which justifies the use of the dipole field as a good approximation [28]. However, taking into account the possible contributions from the multipolar components, especially in the vicinity of the neutron star, we need to extend our pulsar model by superposing the dipole and higher-order multipole fields. A simple extension can be implemented by considering a rotating off-centered dipole, and a number of studies have been carried out regarding a variety of astrophysical consequences of such extension models in pulsar astronomy (see [28] and references therein).¹³ As the simplest model, one can consider ‘quadrupole’ fields, a superposition of dipole and quadrupole fields [24, 25, 27].

The magnetic field of an oblique quadrupole rotator can be written as

$$\begin{aligned} \mathbf{B}_{\text{qd}}(r, \theta, \phi) = & \left[\frac{2\mu_d (\cos \alpha \cos \theta + \sin \alpha \sin \theta \cos \phi)}{r^3} + \frac{\mu_q (3 (\cos \alpha \cos \theta + \sin \alpha \sin \theta \cos \phi)^2 - 1)}{r^4} \right] \mathbf{e}_r \\ & + \left[\frac{\mu_d (\cos \alpha \sin \theta - \sin \alpha \cos \theta \cos \phi)}{r^3} + \frac{2\mu_q (\cos \alpha \sin \theta - \sin \alpha \cos \theta \cos \phi) (\cos \alpha \cos \theta + \sin \alpha \sin \theta \cos \phi)}{r^4} \right] \mathbf{e}_\theta \\ & + \left[\frac{\mu_d \sin \alpha \sin \phi}{r^3} + \frac{2\mu_q \sin \alpha \sin \phi (\cos \alpha \cos \theta + \sin \alpha \sin \theta \cos \phi)}{r^4} \right] \mathbf{e}_\phi. \end{aligned} \tag{40}$$

Here the subscript ‘qd’ on the left-hand side stands for ‘quadrupole’ (hereafter, this will be attached to notations for any quantities affected by the quadrupole field), and μ_d and μ_q denote the magnetic dipole and quadrupole moments, respectively.

The magnetic dipole moment can be expressed as $\mu_d = \pi r_*^2 I$, as produced by a static loop current I of radius of the neutron star r_* , encircling its equator. Similarly, one can express the magnetic quadrupole moment as $\mu_q = 2\chi \pi r_*^3 I = 2\chi r_* \mu_d$, as produced by two identical magnetic dipole loops carrying opposing equal currents I , each of radius r_* , separated by distance χr_* (i.e., anti-Helmholtz

coils), where $\chi > 0$ is a free parameter to determine the ratio between the dipole and quadrupole moments. For example, the magnetic field lines of an oblique quadrupole rotator, with $\chi = 1$, that is, $\mu_q = 2r_* \mu_d$, set for Eq. (40) are illustrated in Fig. 9.

As the magnetic field geometry changes from (5) to (40), the classical propagation vector shall be modified from (6) to

$$\hat{\mathbf{n}}_{[0]\text{qd}} = \beta_{\text{qd}} \hat{\mathbf{B}}_{\text{qd}} + \frac{\boldsymbol{\Omega}_p \times \mathbf{r}}{c}, \tag{41}$$

where $\hat{\mathbf{B}}_{\text{qd}} \equiv \mathbf{B}_{\text{qd}} / |\mathbf{B}_{\text{qd}}|$ and

$$\begin{aligned} \beta_{\text{qd}} \equiv & \left[1 - \left(\frac{\Omega_p r}{c} \right)^2 \sin^2 \theta \left(1 - \frac{\sin^2 \alpha \sin^2 \phi}{f(\theta'; \chi)} \right) \right]^{1/2} \\ & - \frac{\Omega_p r \sin \alpha \sin \theta \sin \phi}{c [f(\theta'; \chi)]^{1/2}}, \end{aligned} \tag{42}$$

with

$$\begin{aligned} f(\theta'; \chi) \equiv & 3 \cos^2 \theta' + 1 + 16\chi \frac{r_*}{r} \cos^3 \theta' + 4\chi^2 \left(\frac{r_*}{r} \right)^2 \\ & \times \left(5 \cos^4 \theta' - 2 \cos^2 \theta' + 1 \right) \end{aligned} \tag{43}$$

and $\cos \theta' \equiv \cos \alpha \cos \theta + \sin \alpha \sin \theta \cos \phi$.

Similarly to Sect. 2.1, taking only the leading order expansions of $\hat{\mathbf{B}}_{\text{qd}}(r_o, \theta_o, \phi)$ and $\beta_{\text{qd}}(r_o, \theta_o, \phi)$ in ϕ from Eqs. (40) and (42), respectively, one can write down the classical propagation vector out of Eq. (41) in Cartesian coordinates as

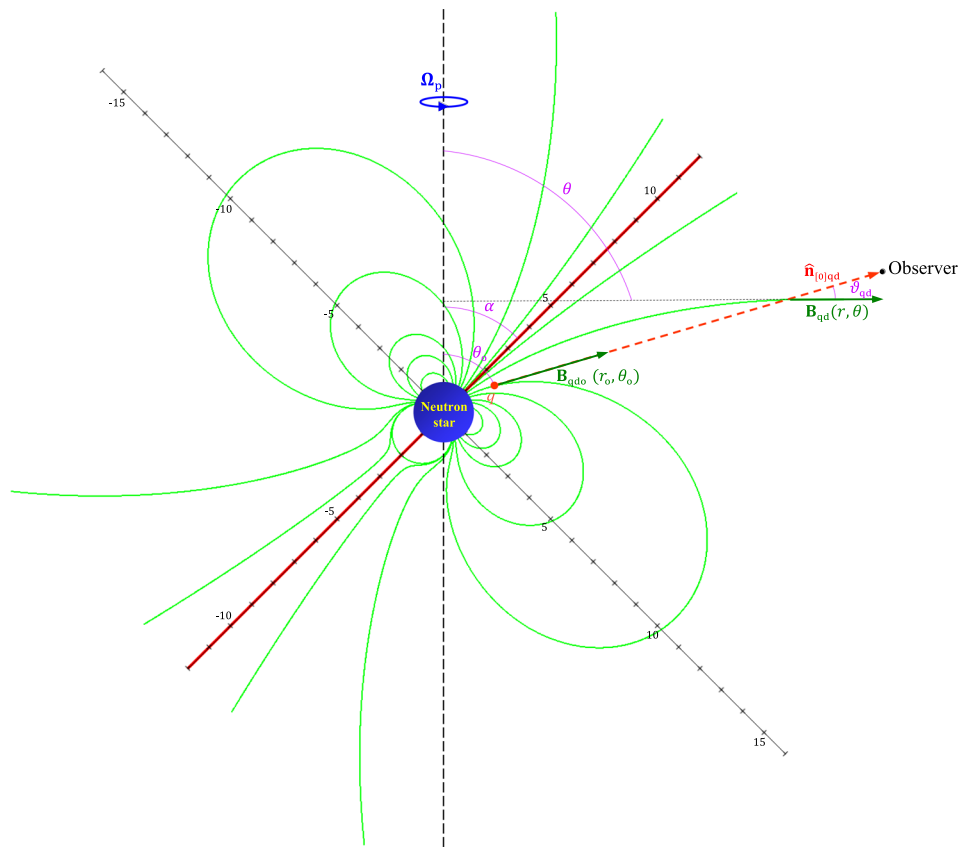
$$\hat{\mathbf{n}}_{[0]\text{qd}} = \hat{n}_{x[0]\text{qd}} \mathbf{e}_x + \hat{n}_{y[0]\text{qd}} \mathbf{e}_y + \hat{n}_{z[0]\text{qd}} \mathbf{e}_z \tag{44}$$

where

$$\begin{aligned} \hat{n}_{x[0]\text{qd}} \approx & [f(\theta_o - \alpha; \chi)]^{-1/2} \left\{ 2 \cos(\theta_o - \alpha) \sin \theta_o \right. \\ & + \sin(\theta_o - \alpha) \cos \theta_o \\ & + 2\chi \frac{r_*}{r_o} \left[\left(3 \cos^2(\theta_o - \alpha) - 1 \right) \sin \theta_o \right. \\ & + \left. \left. 2 \cos(\theta_o - \alpha) \sin(\theta_o - \alpha) \cos \theta_o \right] \right\} \\ & + \mathcal{O} \left(\phi^2, \left(\Omega_p r_o / c \right)^2, \phi \left(\Omega_p r_o / c \right) \right), \end{aligned} \tag{45}$$

¹³ The multipole field structure extended in this way inevitably has the higher-order fields aligned with the dipolar axis. Although the aligned multipole fields might not accurately represent actual field geometries in nature (as illustrated in Ref. [26]), the models would still be useful for estimating roughly the ‘beyond-dipole’ effects in pulsar emission in the near-field regime, as shown in Sect. 3.2.1 later.

Fig. 9 A cross-sectional view of a pulsar magnetosphere with the quadrupole (dipole + quadrupole) magnetic field lines (green) around a neutron star, where the relation between the magnetic dipole and quadrupole moments is set by $\mu_q = 2r_*\mu_d$ for the total field (40). The vertical dashed line (black) and the inclined solid line (red) represent the rotation axis and the magnetic axis, respectively. α between these axes denotes the inclination angle. The scale of the unity in this graph is equivalent to the neutron star radius $\sim 10^6$ cm. The red dashed line represents the trajectory curve of the light ray traced by the propagation vector $\hat{n}_{[0]qd}$ as projected onto the xz -plane



$$\begin{aligned} \hat{n}_{z[0]qd} \approx & [f(\theta_o - \alpha; \chi)]^{-1/2} \left\{ 2 \cos(\theta_o - \alpha) \cos \theta_o \right. \\ & - \sin(\theta_o - \alpha) \sin \theta_o \\ & + 2\chi \frac{r_*}{r_o} \left[(3 \cos^2(\theta_o - \alpha) - 1) \cos \theta_o \right. \\ & \left. \left. - 2 \cos(\theta_o - \alpha) \sin(\theta_o - \alpha) \sin \theta_o \right] \right\} \\ & + \mathcal{O}(\phi^2, (\Omega_p r_o/c)^2, \phi(\Omega_p r_o/c)), \end{aligned} \quad (46)$$

and

$$\begin{aligned} \hat{n}_{y[0]qd} \approx & \frac{\Omega_p}{c} \left\{ [f(\theta_o - \alpha; \chi)]^{-1/2} \sin \alpha \right. \\ & \left. \times \left(1 + 4\chi \frac{r_*}{r_o} \cos(\theta_o - \alpha) \right) s + r_o \sin \theta_o \right\} \\ & + \mathcal{O}(\phi^2, (\Omega_p r_o/c)^2, \phi(\Omega_p r_o/c)), \end{aligned} \quad (47)$$

with $f(\theta_o - \alpha; \chi)$ referring to Eq. (43) for $\theta = \theta_o$ and $\phi = 0$. In association with $\hat{n}_{[0]qd}$, the orthogonal pair of classical mode polarization vectors are determined as

$$\mathbf{e}_{I[0]qd} = \hat{n}_{z[0]qd} \mathbf{e}_x + \hat{n}_{y[0]qd} \mathbf{e}_y - \hat{n}_{x[0]qd} \mathbf{e}_z, \quad (48)$$

$$\begin{aligned} \mathbf{e}_{II[0]qd} = & -(\hat{n}_{x[0]qd} + \hat{n}_{z[0]qd}) \hat{n}_{y[0]qd} \mathbf{e}_x + \mathbf{e}_y \\ & + (\hat{n}_{x[0]qd} - \hat{n}_{z[0]qd}) \hat{n}_{y[0]qd} \mathbf{e}_z, \end{aligned} \quad (49)$$

such that the three vectors, $\hat{n}_{[0]qd}$, $\mathbf{e}_{I[0]qd}$ and $\mathbf{e}_{II[0]qd}$ form an orthonormal basis.

In addition, due to (40) and (44), the angle between the photon trajectory and the local magnetic field line, as defined by Eq. (3) shall be modified. Then we have

$$\begin{aligned} \cos \vartheta_{qd} \approx & [f(\theta_o - \alpha; \chi)]^{-1/2} [f(\theta - \alpha; \chi)]^{-1/2} \\ & \times \left[4 \cos(\theta_o - \alpha) \cos(\theta - \alpha) + \sin(\theta_o - \alpha) \right. \\ & \left. \times \sin(\theta - \alpha) + \chi g_1(r, \theta) + \chi^2 g_2(r, \theta) \right] \\ & + \mathcal{O}(\phi^2, (\Omega_p r_o/c)^2, \phi(\Omega_p r_o/c)), \end{aligned} \quad (50)$$

where

$$\begin{aligned} g_1(r, \theta) = & 4 \frac{r_*}{r_o} \left[(3 \cos^2(\theta_o - \alpha) - 1) \cos(\theta - \alpha) \right. \\ & \left. + \cos(\theta_o - \alpha) \sin(\theta_o - \alpha) \sin(\theta - \alpha) \right] \\ & + 4 \frac{r_*}{r} \left[(3 \cos^2(\theta - \alpha) - 1) \cos(\theta_o - \alpha) \right. \\ & \left. + \cos(\theta - \alpha) \sin(\theta - \alpha) \sin(\theta_o - \alpha) \right], \end{aligned} \quad (51)$$

$$\begin{aligned} g_2(r, \theta) = & 4 \frac{r_*^2}{r_o r} \left[(3 \cos^2(\theta_o - \alpha) - 1) (3 \cos^2(\theta - \alpha) - 1) \right. \\ & \left. + 4 \cos(\theta_o - \alpha) \sin(\theta_o - \alpha) \cos(\theta - \alpha) \sin(\theta - \alpha) \right]. \end{aligned} \quad (52)$$

Now, having \mathbf{B}_{qd} , $\hat{\mathbf{n}}_{[0]\text{qd}}$, $\boldsymbol{\varepsilon}_{\text{I}[0]\text{qd}}$, $\boldsymbol{\varepsilon}_{\text{II}[0]\text{qd}}$ and $\cos \vartheta_{\text{qd}}$ at hand, as given by Eqs. (40), (44), (48), (49) and (50) above, respectively, we modify the evolution equations of the Stokes vector (1) to

$$\frac{d\mathbf{S}}{ds} = k\hat{\boldsymbol{\Omega}}_{\text{qd}} \times \mathbf{S}, \tag{53}$$

where

$$\hat{\boldsymbol{\Omega}}_{\text{qd}} \equiv \frac{\alpha_c}{30\pi} (B_{\text{qd}}/B_c)^2 \sin^2 \vartheta_{\text{qd}} (\mathcal{E}_{\text{Iqd}}^2 - \mathcal{E}_{\text{IIqd}}^2, 2\mathcal{E}_{\text{Iqd}}\mathcal{E}_{\text{IIqd}}, 0). \tag{54}$$

Here $\sin \vartheta_{\text{qd}}$ is defined via (50), and

$$\begin{aligned} \mathcal{E}_{\text{Iqd}} &= -\hat{\mathbf{B}}_{\text{qd}} \cdot (\hat{\mathbf{n}}_{[0]\text{qd}} \times \boldsymbol{\varepsilon}_{\text{I}[0]\text{qd}}) \\ &\approx [f(\theta_0 - \alpha; \chi)]^{-1/2} [f(\theta - \alpha; \chi)]^{-1/2} \\ &\quad \times \left\{ \left[2 \cos(\theta_0 - \alpha) + 2\chi \frac{r_*}{r_0} (3 \cos^2(\theta_0 - \alpha) - 1) \right] \right. \\ &\quad \times \left[2 \cos(\theta - \alpha) + 2\chi \frac{r_*}{r} (3 \cos^2(\theta - \alpha) - 1) \right] \\ &\quad \left. + \sin(\theta_0 - \alpha) \left[1 + 4\chi \frac{r_*}{r_0} \cos(\theta_0 - \alpha) \right] \sin(\theta - \alpha) \right. \\ &\quad \left. \times \left[1 + 4\chi \frac{r_*}{r} \cos(\theta - \alpha) \right] \right\} \hat{n}_{y[0]\text{qd}} \\ &\quad - \mathcal{E}_{\text{IIqd}} \hat{n}_{y[0]\text{qd}} - \frac{\Omega_p \sin \alpha}{c} [f(\theta - \alpha; \chi)]^{-1/2} \\ &\quad \times \left[1 + 4\chi \frac{r_*}{r} \cos(\theta - \alpha) \right] s \\ &\quad + \mathcal{O}(\phi^2, (\Omega_p r_0/c)^2, \phi(\Omega_p r_0/c)), \end{aligned} \tag{55}$$

$$\begin{aligned} \mathcal{E}_{\text{IIqd}} &= -\hat{\mathbf{B}}_{\text{qd}} \cdot (\hat{\mathbf{n}}_{[0]\text{qd}} \times \boldsymbol{\varepsilon}_{\text{II}[0]\text{qd}}) \\ &\approx [f(\theta_0 - \alpha; \chi)]^{-1/2} [f(\theta - \alpha; \chi)]^{-1/2} \\ &\quad \times \left\{ \left[2 \cos(\theta - \alpha) + 2\chi \frac{r_*}{r} (3 \cos^2(\theta - \alpha) - 1) \right] \right. \\ &\quad \times \sin(\theta_0 - \alpha) \left[1 + 4\chi \frac{r_*}{r_0} \cos(\theta_0 - \alpha) \right] \\ &\quad \left. - \left[2 \cos(\theta_0 - \alpha) + 2\chi \frac{r_*}{r_0} (3 \cos^2(\theta_0 - \alpha) - 1) \right] \right. \\ &\quad \left. \times \sin(\theta - \alpha) \left[1 + 4\chi \frac{r_*}{r} \cos(\theta - \alpha) \right] \right\} \\ &\quad + \mathcal{O}(\phi^2, (\Omega_p r_0/c)^2, \phi(\Omega_p r_0/c)), \end{aligned} \tag{56}$$

with $f(\theta - \alpha; \chi)$ referring to Eq. (43) for $\phi = 0$.

3.2 Solving the evolution equations

From Eq. (54) one can write out the non-zero components of the birefringent vector:

$$\hat{\boldsymbol{\Omega}}_{1\text{qd}} \approx -\eta B_{\text{qd}}^2 \sin^2 \vartheta_{\text{qd}} \mathcal{E}_{\text{IIqd}}^2$$

$$+ \mathcal{O}(\phi^2, (\Omega_p r_0/c)^2, \phi(\Omega_p r_0/c)), \tag{57}$$

$$\begin{aligned} \hat{\boldsymbol{\Omega}}_{2\text{qd}} &\approx 2\eta B_{\text{qd}}^2 \sin^2 \vartheta_{\text{qd}} \mathcal{E}_{\text{Iqd}} \mathcal{E}_{\text{IIqd}} \\ &\quad + \mathcal{O}(\phi^2, (\Omega_p r_0/c)^2, \phi(\Omega_p r_0/c)), \end{aligned} \tag{58}$$

where $\eta \equiv \alpha_c / (30\pi B_c^2)$, and \mathcal{E}_{Iqd} and $\mathcal{E}_{\text{IIqd}}$ refer to Eqs. (55) and (56), respectively, and $\sin \vartheta_{\text{qd}}$ is defined via Eq. (50), while

$$B_{\text{qd}} = \frac{B_{\text{max}} r_*^3 [f(\theta - \alpha; \chi)]^{1/2}}{2(1 + 2\chi)(x^2 + z^2)^{3/2}} \tag{59}$$

due to Eq. (40), with B_{max} being the maximum magnetic field intensity at the polar cap, r_* being the neutron star radius and $f(\theta - \alpha; \chi)$ referring to Eq. (43) for $\phi = 0$. Having Eqs. (57) and (58) at hand, we solve a system of differential equations, i.e., the evolution equations of the Stokes vector, written out in component form from (53):

$$\dot{S}_1(s) = k\hat{\boldsymbol{\Omega}}_{2\text{qd}}(s) S_3(s), \tag{60}$$

$$\dot{S}_2(s) = -k\hat{\boldsymbol{\Omega}}_{1\text{qd}}(s) S_3(s), \tag{61}$$

$$\dot{S}_3(s) = k[\hat{\boldsymbol{\Omega}}_{1\text{qd}}(s) S_2(s) - \hat{\boldsymbol{\Omega}}_{2\text{qd}}(s) S_1(s)]. \tag{62}$$

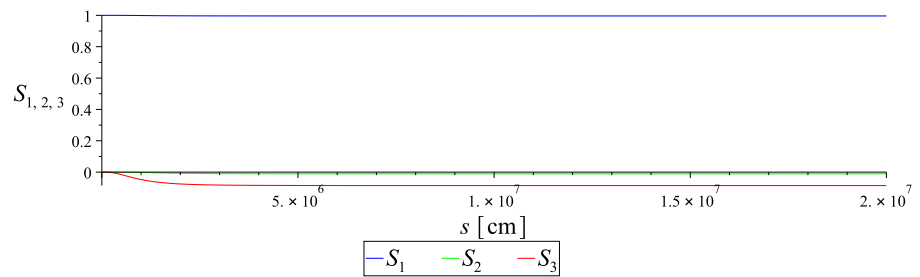
3.2.1 Examples

We consider again X-ray emissions from the same three RPPs as in Sect. 2.2.1: (i') one with $B_{\text{max}} \approx 10^{12}$ G and $\Omega_p \approx 392.7$ Hz ($P \approx 0.016$ s), (ii') another with $B_{\text{max}} \approx 5.6 \times 10^{12}$ G and $\Omega_p \approx 22.28$ Hz ($P \approx 0.282$ s), (iii') the third with $B_{\text{max}} \approx 5.0 \times 10^{13}$ G and $\Omega_p \approx 19.6$ Hz ($P \approx 0.32$ s). Again, for all three, we assume $r_0 = 2r_* \approx 2 \times 10^6$ cm, $\theta_0 = 60^\circ$, $\alpha = 45^\circ$, $\eta \approx 3.97 \times 10^{-32}$ and $\omega \approx 2\pi \times 10^{18}$ Hz ($k \approx 2.0958 \times 10^8$ cm $^{-1}$). However, unlike the dipole pulsars as in Sect. 2.2.1, quadrupole pulsars can be modeled by setting the value of an arbitrary parameter χ to determine the ratio between the magnetic dipole and quadrupole moments; we choose two values, $\chi = 1.585$ and 0.85 to model each RPP in our analysis here.¹⁴

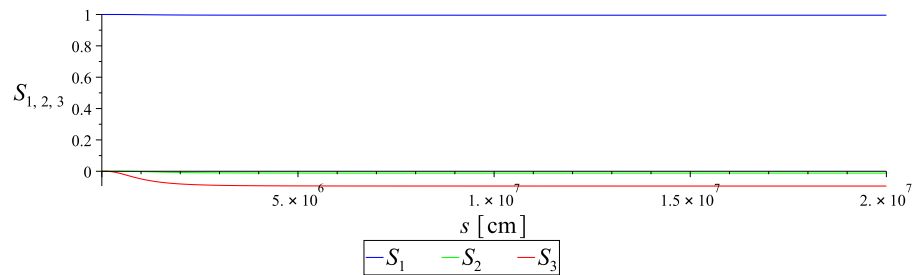
In Figs. 10, 11 and 12 are plotted our numerical solutions of Eqs. (60)–(62) for the Stokes vectors in Examples (i'), (ii') and (iii'), respectively. Also, in Fig. 13 we present the solutions as represented on the Poincaré sphere for $\chi = 1.585$

¹⁴ The values $\chi = 1.585$ and 0.85 have been determined such that they optimize $\hat{\Omega}_{1\text{qd}}(s; \chi) \leq 0$ and $\hat{\Omega}_{2\text{qd}}(s; \chi) \geq 0$, respectively. That is to say, the optimal values of $\hat{\Omega}_{1\text{qd}}(\text{min})$ and $\hat{\Omega}_{2\text{qd}}(\text{max})$ are found at ($s \approx 8.2444 \times 10^5$ cm; $\chi \approx 1.585$) and ($s \approx 6.3588 \times 10^5$ cm; $\chi \approx 0.85$), respectively, which are determined from $\partial \hat{\Omega}_{1\text{qd}}(s; \chi) / \partial s = \partial \hat{\Omega}_{1\text{qd}}(s; \chi) / \partial \chi = 0$ and $\partial \hat{\Omega}_{2\text{qd}}(s; \chi) / \partial s = \partial \hat{\Omega}_{2\text{qd}}(s; \chi) / \partial \chi = 0$, respectively. In consideration of Eqs. (60)–(62), these values will maximize the effects of birefringence on our evolution system.

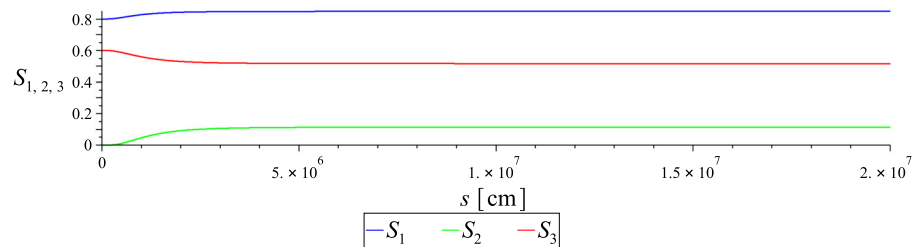
Fig. 10 For Example (i'): the evolution of the Stokes vector $\mathbf{S}(s) = (S_1(s), S_2(s), S_3(s))$, $0 \leq s \leq 20r_*$ ($\approx 2 \times 10^7$ cm), for the X-ray emissions from the quadrupole pulsar with $B_{\max} \approx 10^{12}$ G and $\Omega_p \approx 392.7$ Hz ($P \approx 0.016$ s)



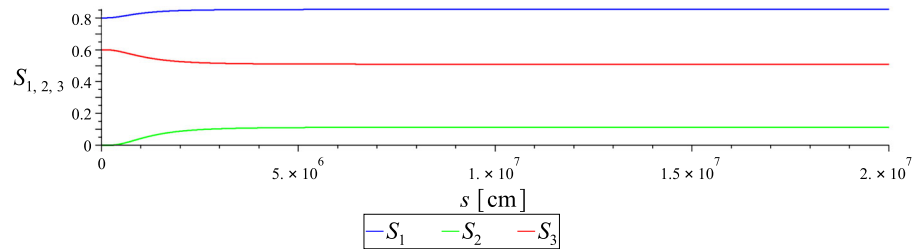
(a) With $\mathbf{S}(0) = (1, 0, 0)$ and $\chi = 1.585$



(b) With $\mathbf{S}(0) = (1, 0, 0)$ and $\chi = 0.85$



(c) With $\mathbf{S}(0) = (0.8, 0, 0.6)$ and $\chi = 1.585$

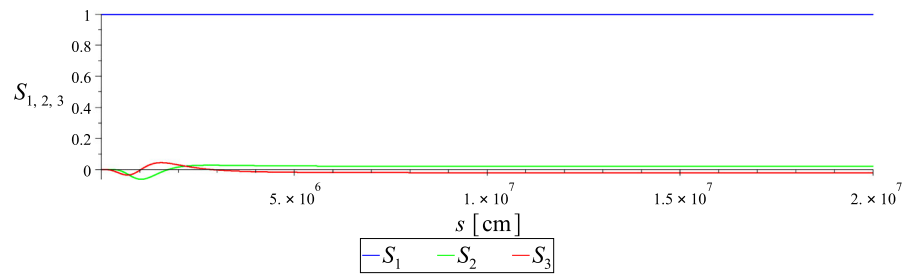


(d) With $\mathbf{S}(0) = (0.8, 0, 0.6)$ and $\chi = 0.85$

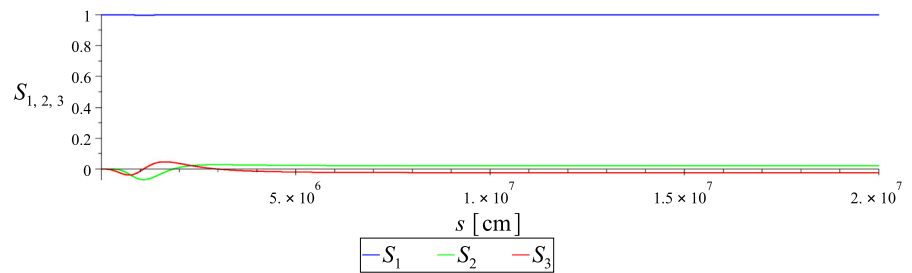
only; there is little difference in the representations of solutions between $\chi = 1.585$ and 0.85 cases. The solutions represented by the three magenta loci and the three light blue loci in Fig. 13 correspond to Figs. 10a, 11a, 12a and Figs. 10c, 11c, 12c, respectively. In Fig. 10 for Example (i'), where B_{\max} is relatively weak among the three RPPs, general patterns of polarization evolution are shown to be nearly the same for $\chi = 1.585$ and 0.85 , and to be almost the same even to the dipole case as given by Fig. 3 for Example (i) in Sect. 2.2.1; it is also confirmed by comparing the representations in Figs. 6a and 13a. In contrast, in Fig. 11 for Example (ii'), where B_{\max} is intermediate among the three RPPs, general patterns of polarization evolution are shown to be nearly the same for

$\chi = 1.585$ and 0.85 , but to be noticeably different from the dipole case as given by Fig. 4 for Example (ii) in Sect. 2.2.1; comparing the representations in Figs. 6b and 13b, the number of cycles appears to become nearly doubled (from half a cycle to one cycle). However, in Fig. 12 for Example (iii'), where B_{\max} is the strongest among the three RPPs, general patterns of polarization evolution are shown to be similar for $\chi = 1.585$ and 0.85 , with noticeable differences in phase, but to be significantly different from the dipole case as given by Fig. 5 for Example (iii) in Sect. 2.2.1; the plots appear to be much denser in the early part of evolution in Fig. 12 than in Fig. 5, as the polarization states oscillate much more frequently in the quadrupole field than in the dipole field,

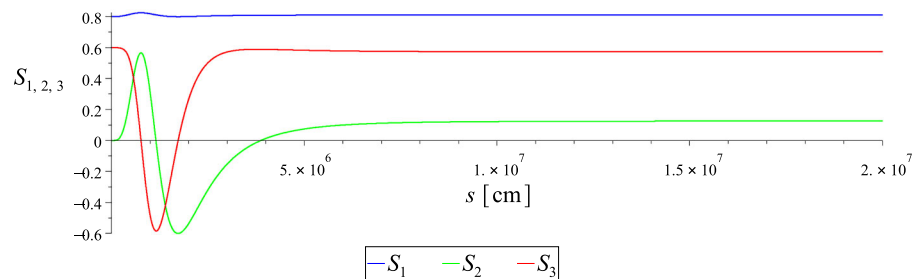
Fig. 11 For Example (ii'): the evolution of the Stokes vector $\mathbf{S}(s) = (S_1(s), S_2(s), S_3(s))$, $0 \leq s \leq 20r_*$ ($\approx 2 \times 10^7$ cm), for the X-ray emissions from the quadrupole pulsar with $B_{\max} \approx 5.6 \times 10^{12}$ G and $\Omega_p \approx 22.28$ Hz ($P \approx 0.282$ s)



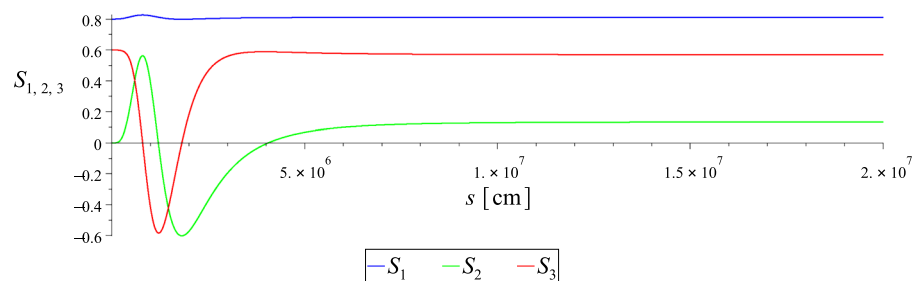
(a) With $\mathbf{S}(0) = (1, 0, 0)$ and $\chi = 1.585$



(b) With $\mathbf{S}(0) = (1, 0, 0)$ and $\chi = 0.85$



(c) With $\mathbf{S}(0) = (0.8, 0, 0.6)$ and $\chi = 1.585$



(d) With $\mathbf{S}(0) = (0.8, 0, 0.6)$ and $\chi = 0.85$

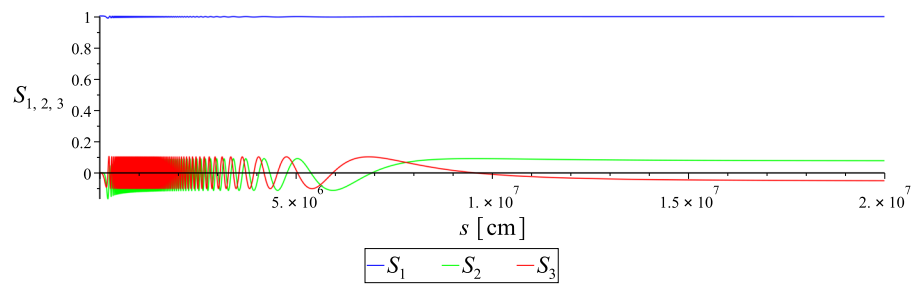
which can also be confirmed by comparing the representations in Figs. 6c and 13c.

4 Conclusions and discussion

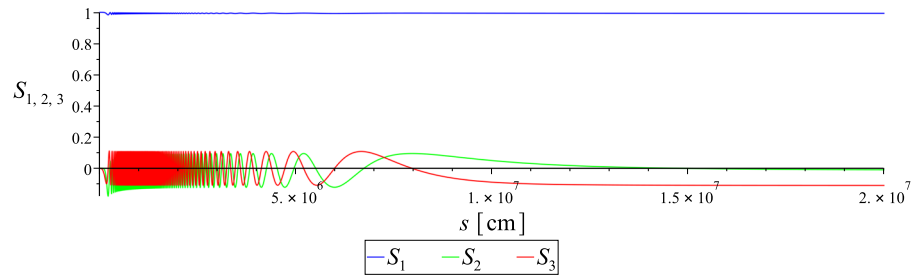
We have investigated the evolution of polarization states of pulsar emission under the quantum refraction effects, combined with the dependence on the emission frequency, for both dipole and quadrupole pulsar models. To this end, we have solved a system of evolution equations of the Stokes

vector given by (1) (or by (23)–(25)) and (53) (or by (60)–(62)) in the dipole and quadrupole cases, respectively, for three examples of RPPs at a fixed frequency for specific emissions (e.g., X-rays as in sections 2.2.1, 2.2.2 and 3.2.1). Our main results are presented by Figs. 3, 4, 5 and 10, 11, 12 in the dipole and quadrupole cases, respectively, from numerical solutions and in part from perturbative solutions. Also, we have replaced the birefringent vector with some approximate models as in Fig. 7 to solve the evolution equations analytically in the dipole case, and obtained the results as presented by Fig. 8. It is noteworthy that at a fixed frequency of emis-

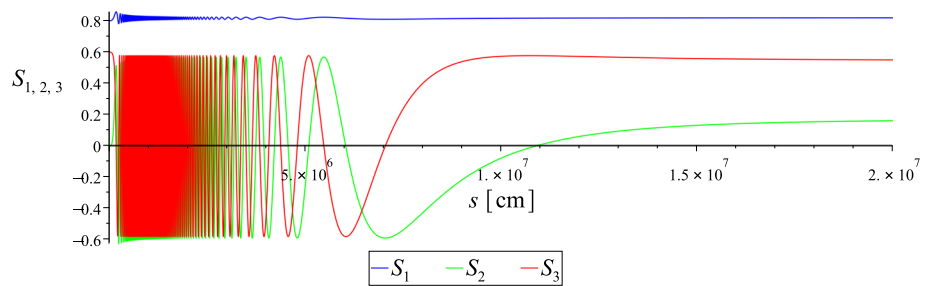
Fig. 12 For Example (iii'): the evolution of the Stokes vector $\mathbf{S}(s) = (S_1(s), S_2(s), S_3(s))$, $0 \leq s \leq 20r_* (\approx 2 \times 10^7 \text{ cm})$, for the X-ray emissions from the quadrupole pulsar with $B_{\text{max}} \approx 5.0 \times 10^{13} \text{ G}$ and $\Omega_p \approx 19.6 \text{ Hz}$ ($P \approx 0.32 \text{ s}$)



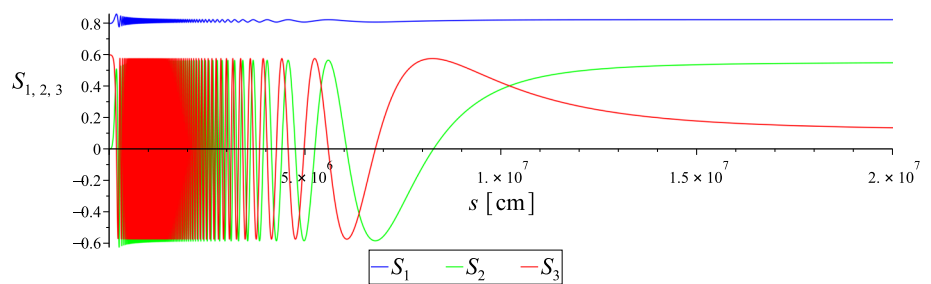
(a) With $\mathbf{S}(0) = (1, 0, 0)$ and $\chi = 1.585$



(b) With $\mathbf{S}(0) = (1, 0, 0)$ and $\chi = 0.85$

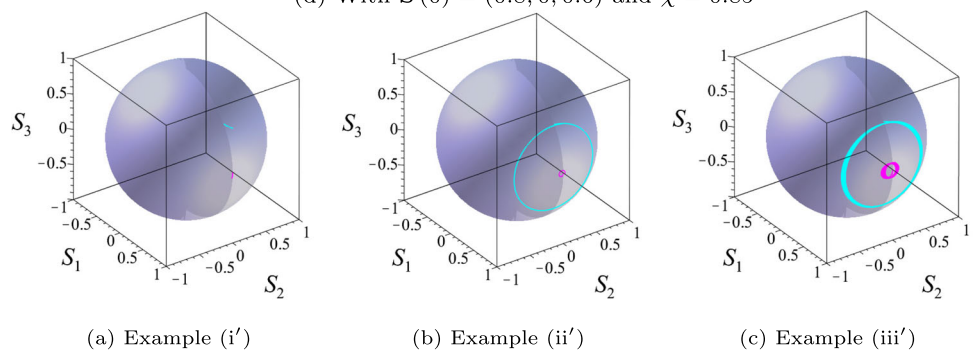


(c) With $\mathbf{S}(0) = (0.8, 0, 0.6)$ and $\chi = 1.585$



(d) With $\mathbf{S}(0) = (0.8, 0, 0.6)$ and $\chi = 0.85$

Fig. 13 Representations of the Stokes vectors from Examples (i')–(iii') for $\chi = 1.585$ on the Poincaré sphere. The loci imply patterns of the polarization evolution in terms of oscillation



(a) Example (i')

(b) Example (ii')

(c) Example (iii')

sion the evolution of the Stokes vector largely exhibits three different patterns, depending on the magnitudes of the birefringent vector, in which the magnetic field strength is a dominant factor: (i) fractionally oscillatory – monotonic, or (ii) half-oscillatory, or (iii) highly oscillatory behaviors. These features are shown by the numerical solutions in Figs. 3, 4, 5, 6, and also confirmed by the approximate analytical solutions in Fig. 8. In addition, we have examined how the aforementioned features change in the quadrupole case.

This study is centered on solving the evolution equations for polarization states (1), wherein the birefringent vector that contains all information about the quantum refraction effects, coupled to the frequency of pulsar emission, acts on the Stokes vector; the evolution results from the combination of the quantum refraction effects and the frequency dependence of the emission. This is a major difference from our previous work [23], wherein the same effects have no connection to the emission frequency; the work solely focuses on the quantum refraction effects on the propagation and polarization vectors in pulsar emission, with no reference to other properties, such as the emission frequency. In this regard, it is worthwhile to draw comparison between the two quantities, the polarization vector and the Stokes vector, both of which are used to describe polarization states. The polarization vector is defined directly from the radiative electric field vector (i.e., the unit electric field vector), and it is parallel-transported along the the propagation vector; usually, we consider such two vectors orthogonal to each other and to the propagation vector to define an orthonormal basis consisting of the three vectors. In contrast, the Stokes vector is defined from Stokes parameters which are built out of the radiative electric field vector [45]. The representation of the Stokes vector is abstract in the sense that it is a vector defined on the Poincaré sphere. The Stokes vector is not parallel-transported along the the propagation vector, but can still be defined along the propagation vector as the two polarization vectors move along it; hence, it can be parameterized by s to represent polarization states along the photon trajectory. However, the Stokes vector has a crucial advantage over the polarization vector in representing polarization states in some astrophysical studies like this: it can be directly estimated from polarimetric measurements and accommodate depolarization effects due to incomplete coherence and random processes during the photon propagation [46].

Our results in this study may be of some significance for the currently operating and planned X-ray space telescopes: Imaging X-ray Polarimetry Explorer (IXPE) [14], X-ray Polarimeter Satellite (XPoSat) [15], the enhanced X-ray Timing and Polarimetry mission (eXTP) [16] and the Compton Telescope project [17]. These telescopes measure the polarization of the X-rays from energetic compact objects such as magnetars and black holes to unveil their geometry and physical environment in detail. Several magnetars

observed by IXPE have been estimated to have overcritical field strengths [47,48]. Furthermore, a recent measurement of the X-ray polarization of the magnetar 4U 0142+61 has shown that the polarization degree and angle change as a function of X-ray energy, the interpretation of which has led to two competing scenarios about the X-ray emission of the magnetar [47,49]. In fact, a full analysis of the polarimetry data would require a physical model that comprehensively incorporates the properties regarding the polarization of surface emission, the photon propagation through magnetized plasmas, birefringence due to a magnetized quantum vacuum, and gravitational effects on photon propagation [50,51].

In this study, we have focused on vacuum birefringence as it is one of the most significant phenomenological issues to be tested by the X-ray polarimetry in practice. When the magnetic field is sufficiently strong and slowly varying, the polarization states evolve due to vacuum birefringence; that is, the Stokes vector components change during the photon propagation within the so-called polarization-limiting radius [29,34], which can be several to a couple dozen neutron-star radii, depending on the magnetic field strength at the surface of a neutron star and the emission frequency. However, beyond the polarization-limiting radius, the polarization states ‘freeze’, remaining the same until finally being observed through polarimetry [34,51]. The new features of the polarization evolution presented in our study, such as the three different oscillatory patterns of the Stokes vectors and the effects of the possible contributions from the multipolar components may all closely concern the observation through the X-ray polarimetry, and therefore should be taken into proper consideration for a more accurate model for pulsar emission.

Effects of gravitation have not been considered in this study. However, close to the neutron star, where gravitation due to the neutron star mass may not be negligible, its effects must be taken into account in our analysis. Then, basically, the following shall be redefined in curved spacetime: (1) the QED one-loop effective Lagrangian, (2) the refractive index for the photon propagation, (3) the magnetic field geometry in the magnetosphere, (4) the radiative electric field due to a charge moving along a magnetic field line, (5) the photon trajectory. All these have not been rigorously dealt with in previous studies. In this regard, inclusion of the gravitational effects will involve non-trivial and immense analyses, and therefore shall be conducted for a long-term plan in our future studies.

Acknowledgements D.-H.K was supported by the Basic Science Research Program through the National Research Foundation of Korea (NRF) funded by the Ministry of Education (NRF-2021R111A1A01054781). C.M.K. was supported by Ultrashort Quantum Beam Facility operation program (140011) through APRI, GIST and GIST Research Institute (GRI) grant funded by GIST. S.P.K. was also in part supported

by National Research Foundation of Korea (NRF) funded by the Ministry of Education (NRF-2019R1I1A3A01063183).

Data Availability Statement Data will be made available on reasonable request. [Authors’ comment: xxx].

Code Availability Statement This manuscript has no associated code/software. [Authors’ comment: xxx].

Open Access This article is licensed under a Creative Commons Attribution 4.0 International License, which permits use, sharing, adaptation, distribution and reproduction in any medium or format, as long as you give appropriate credit to the original author(s) and the source, provide a link to the Creative Commons licence, and indicate if changes were made. The images or other third party material in this article are included in the article’s Creative Commons licence, unless indicated otherwise in a credit line to the material. If material is not included in the article’s Creative Commons licence and your intended use is not permitted by statutory regulation or exceeds the permitted use, you will need to obtain permission directly from the copyright holder. To view a copy of this licence, visit <http://creativecommons.org/licenses/by/4.0/>.
Funded by SCOAP³.

Appendix A The classical Stokes vector

Consider a particle with a charge q moving along a curved trajectory (a magnetic field line). Then the curvature radiation due to this can be expressed by the electric field:

$$\mathbf{E}(t) = \frac{q}{c|\mathbf{r} - \boldsymbol{\xi}(t_{\text{ret}})|} \frac{\mathbf{n} \times \left[\left(\mathbf{n} - \frac{\dot{\boldsymbol{\xi}}(t_{\text{ret}})}{c} \right) \times \frac{\ddot{\boldsymbol{\xi}}(t_{\text{ret}})}{c} \right]}{\left(1 - \frac{\dot{\boldsymbol{\xi}}(t_{\text{ret}})}{c} \cdot \mathbf{n} \right)^3}, \quad (\text{A1})$$

where $t_{\text{ret}} \equiv t - r/c$ is the retarded time, $\boldsymbol{\xi}$ represents the particle’s trajectory, \mathbf{n} is the propagation direction of the radiation, and an over-dot $\dot{}$ denotes differentiation with respect to t . In a suitably chosen Cartesian frame, by setting $\boldsymbol{\xi}(t_{\text{ret}}) = \rho(\sin(\beta ct_{\text{ret}}/\rho), 0, \cos(\beta ct_{\text{ret}}/\rho))$, with ρ being the radius of curvature of the particle’s trajectory, and $\mathbf{n} = (\cos \varphi, \sin \varphi, 0)$, with φ being the angle measured from the x -axis to the plane of the particle’s motion, we can construct a simple toy model for pulse profiles of pulsar curvature emission as described below [37].

One can express Stokes parameters out of the radiation field (A1), which describe its polarization properties [52]:

$$\begin{aligned} I &= \tilde{E}_{\parallel}^* \tilde{E}_{\parallel} + \tilde{E}_{\perp}^* \tilde{E}_{\perp} \\ &= \mathcal{E}_0^2 \omega^2 \left[(\delta^2 + \varphi^2)^2 \text{K}_{2/3}^2 \left(\frac{\rho\omega}{3\beta c} (\delta^2 + \varphi^2)^{3/2} \right) \right. \\ &\quad \left. + \varphi^2 (\delta^2 + \varphi^2) \text{K}_{1/3}^2 \left(\frac{\rho\omega}{3\beta c} (\delta^2 + \varphi^2)^{3/2} \right) \right], \quad (\text{A2}) \end{aligned}$$

$$\begin{aligned} Q &= \tilde{E}_{\parallel} \tilde{E}_{\parallel} - \tilde{E}_{\perp} \tilde{E}_{\perp} \\ &= \mathcal{E}_0^2 \omega^2 \left[(\delta^2 + \varphi^2)^2 \text{K}_{2/3}^2 \left(\frac{\rho\omega}{3\beta c} (\delta^2 + \varphi^2)^{3/2} \right) \right. \\ &\quad \left. - \varphi^2 (\delta^2 + \varphi^2) \text{K}_{1/3}^2 \left(\frac{\rho\omega}{3\beta c} (\delta^2 + \varphi^2)^{3/2} \right) \right], \quad (\text{A3}) \end{aligned}$$

$$U = \tilde{E}_{\parallel} \tilde{E}_{\perp} + \tilde{E}_{\perp} \tilde{E}_{\parallel}^* = 0, \quad (\text{A4})$$

$$\begin{aligned} V &= -i \left(\tilde{E}_{\parallel}^* \tilde{E}_{\perp} - \tilde{E}_{\parallel} \tilde{E}_{\perp}^* \right) \\ &= -2\mathcal{E}_0^2 \omega^2 \varphi (\delta^2 + \varphi^2)^{3/2} \text{K}_{2/3} \left(\frac{\rho\omega}{3\beta c} (\delta^2 + \varphi^2)^{3/2} \right) \\ &\quad \times \text{K}_{1/3} \left(\frac{\rho\omega}{3\beta c} (\delta^2 + \varphi^2)^{3/2} \right), \quad (\text{A5}) \end{aligned}$$

where \tilde{E}_{\parallel} and \tilde{E}_{\perp} denote the components of the Fourier transform $\tilde{\mathbf{E}}(\omega) = \tilde{E}_{\parallel}(\omega) \mathbf{e}_z + \tilde{E}_{\perp}(\omega) \mathbf{e}_y = \int_{-\infty}^{\infty} \mathbf{E}(t) \exp(i\omega t) dt$, expressed in the Cartesian frame, and $*$ means the complex conjugate, and $\mathcal{E}_0 = q\beta / (2\sqrt{3}\pi^2 r\rho)$, and $\delta \equiv \gamma^{-1} = (1 - \beta^2)^{1/2} \ll 1$ is the half-angle of the beam emission, and $\text{K}_{1/3}$ and $\text{K}_{2/3}$ denote the modified Bessel functions of the second kind. With regard to the polarization state of the radiation field, I is a measure of the total intensity, Q and U jointly describe the linear polarization, and V describes the circular polarization. These parameters can be plotted as functions of the phase angle φ , where $\varphi \leq \delta \ll 5^\circ$ usually, to simulate the pulse profiles of pulsar emission theoretically.

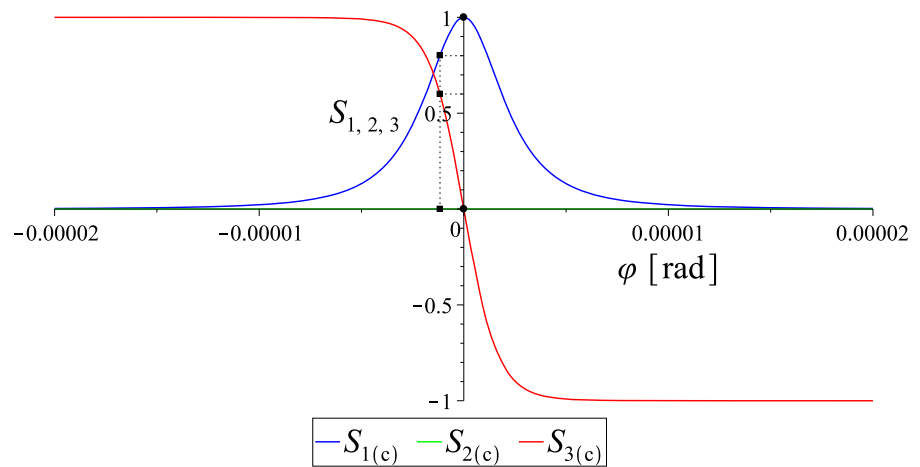
Out of the Stokes parameters, one can define the Stokes vector $\mathbf{S} = (S_1, S_2, S_3) \equiv (Q/I, U/I, V/I)$ and express it using (A2)–(A5):

$$S_1 = \frac{(\delta^2 + \varphi^2) \text{K}_{2/3}^2 \left(\frac{\rho\omega}{3\beta c} (\delta^2 + \varphi^2)^{3/2} \right) - \varphi^2 \text{K}_{1/3}^2 \left(\frac{\rho\omega}{3\beta c} (\delta^2 + \varphi^2)^{3/2} \right)}{(\delta^2 + \varphi^2) \text{K}_{2/3}^2 \left(\frac{\rho\omega}{3\beta c} (\delta^2 + \varphi^2)^{3/2} \right) + \varphi^2 \text{K}_{1/3}^2 \left(\frac{\rho\omega}{3\beta c} (\delta^2 + \varphi^2)^{3/2} \right)}, \quad (\text{A6})$$

$$S_2 = 0, \quad (\text{A7})$$

$$S_3 = -\frac{2\varphi (\delta^2 + \varphi^2)^{1/2} \text{K}_{2/3} \left(\frac{\rho\omega}{3\beta c} (\delta^2 + \varphi^2)^{3/2} \right) \text{K}_{1/3} \left(\frac{\rho\omega}{3\beta c} (\delta^2 + \varphi^2)^{3/2} \right)}{(\delta^2 + \varphi^2) \text{K}_{2/3}^2 \left(\frac{\rho\omega}{3\beta c} (\delta^2 + \varphi^2)^{3/2} \right) + \varphi^2 \text{K}_{1/3}^2 \left(\frac{\rho\omega}{3\beta c} (\delta^2 + \varphi^2)^{3/2} \right)}. \quad (\text{A8})$$

Fig. 14 The classical Stokes vector $\mathbf{S}_{(c)}(\varphi) = (S_{1(c)}(\varphi), S_{2(c)}(\varphi), S_{3(c)}(\varphi))$ plotted against the phase angle φ . Its initial values $\mathbf{S}(\varphi = 0) = (1, 0, 0)$ and $\mathbf{S}(\varphi \approx -1.16 \times 10^{-6} \text{ rad}) = (0.8, 0, 0.6)$ are marked by solid circles and solid boxes, respectively



In Fig. 14 is plotted the classical Stokes vector against the phase angle φ , where we have set, for example, $\delta \approx 10^{-8}$, $\rho \approx 10^8 \text{ cm}$, $\beta \approx 1$ and $\omega \approx 2\pi \times 10^{18} \text{ Hz}$ to model pulse profiles of X-ray pulsar emission. Here the initial values for the Stokes vector, $\mathbf{S}(\varphi = 0) = (1, 0, 0)$ and $\mathbf{S}(\varphi \approx -1.16 \times 10^{-6} \text{ rad}) = (0.8, 0, 0.6)$, as in the examples given in Sect. 2.2.1, are marked by solid circles and solid boxes, respectively.

Appendix B Approximate analytical solutions to evolution equations

Substituting Eq. (30) into Eqs. (23)–(25), the evolution equations can be reduced as follows: For $0 \leq s \leq 20r_*$,

$$\dot{S}_1(s) \approx -ka_2 s^{\frac{p+1}{p}} e^{-bs} S_3(s), \tag{B1}$$

$$\dot{S}_2(s) \approx ka_1 s^{\frac{p+1}{p}} e^{-bs} S_3(s), \tag{B2}$$

$$\ddot{S}_3(s) - \left(\frac{p+1}{ps} - b\right) \dot{S}_3(s) + k^2(a_1^2 + a_2^2) \left(s^{\frac{p+1}{p}} e^{-bs}\right)^2 \times S_3(s) \approx 0. \tag{B3}$$

First, we solve Eq. (B3) for $S_3(s)$, and then using this solution, obtain $S_1(s)$ and $S_2(s)$, by integrating Eqs. (B1) and (B2), respectively:

$$S_3(s) \approx S_0 \sin(\Psi(s; p) + \delta), \tag{B4}$$

$$S_1(s) \approx \frac{a_2 S_0}{\sqrt{a_1^2 + a_2^2}} \cos(\Psi(s; p) + \delta) + S_{1o}, \tag{B5}$$

$$S_2(s) \approx -\frac{a_1 S_0}{\sqrt{a_1^2 + a_2^2}} \cos(\Psi(s; p) + \delta) + S_{2o}, \tag{B6}$$

where

$$\Psi(s; p) \equiv k\sqrt{a_1^2 + a_2^2} b^{-\frac{4p+1}{2p}} s^{\frac{1}{2p}} e^{-\frac{1}{2}bs}$$

$$\times \left[M_{\frac{1}{2p}, \frac{p+1}{2p}}(bs) - M_{\frac{2p+1}{2p}, \frac{p+1}{2p}}(bs) \right], \tag{B7}$$

and $M_{\kappa, \mu}(z)$ denotes a Whittaker function of the first kind. Here employing the identity $S_1^2(s) + S_2^2(s) + S_3^2(s) = 1$ (conservation of the degree of polarization), one can specify S_{1o} and S_{2o} in terms of a_1, a_2 and a constant C , and establish a relation between S_0 and C :

$$S_{1o} = \frac{Ca_1}{\sqrt{a_1^2 + a_2^2}}, \quad S_{2o} = \frac{Ca_2}{\sqrt{a_1^2 + a_2^2}}, \quad S_0^2 + C^2 = 1. \tag{B8}$$

Then S_0, C and δ are determined by matching the initial value of the Stokes vector $\mathbf{S}(0) = (S_1(0), S_2(0), S_3(0))$ with Eqs. (B4)–(B6) evaluated at $s = 0$.

References

1. W. Heisenberg, H. Euler, Folgerungen aus der Diracschen Theorie des Positrons. *Z. Phys.* **98**(11–12), 714 (1936). <https://doi.org/10.1007/BF01343663>
2. J. Schwinger, On gauge invariance and vacuum polarization. *Phys. Rev.* **82**(5), 664–679 (1951). <https://doi.org/10.1103/PhysRev.82.664>
3. P. Mészáros, *High-Energy Radiation from Magnetized Neutron Stars. Astrophysics/Physics* (University of Chicago Press, Chicago, 1992). <https://books.google.co.kr/books?id=BVY7gEs1IYC>
4. C.M. Kim, S.P. Kim, Vacuum birefringence at one-loop in a supercritical magnetic field superposed with a weak electric field and application to pulsar magnetosphere. *Eur. Phys. J. C* **83**(2), 104 (2023). <https://doi.org/10.1140/epjc/s10052-023-11243-1>
5. R. Ruffini, G. Vereshchagin, S.-S. Xue, Electron-positron pairs in physics and astrophysics: from heavy nuclei to black holes. *Phys. Rep.* **487**(1–4), 1–140 (2010). <https://doi.org/10.1016/j.physrep.2009.10.004>
6. A. Fedotov, A. Ilderton, F. Karbstein, B. King, D. Seipt, H. Taya, G. Torgrimsson, Advances in QED with intense background fields. *Phys. Rep.* **1010**, 1–138 (2023). <https://doi.org/10.1016/j.physrep.2023.01.003>
7. K. Hattori, K. Itakura, S. Ozaki, Strong-field physics in QED and QCD: from fundamentals to applications. *Prog. Part. Nucl. Phys.* **133**, 104068 (2023). <https://doi.org/10.1016/j.pnpnp.2023.104068>

8. A. Ejlli, F. Della Valle, U. Gastaldi, G. Messineo, R. Pengo, G. Ruoso, G. Zavattini, The PVLAS experiment: a 25 year effort to measure vacuum magnetic birefringence. *Phys. Rep.* **871**, 1–74 (2020). <https://doi.org/10.1016/j.physrep.2020.06.001>
9. F. Karbstein, C. Sundqvist, K.S. Schulze, I. Uschmann, H. Gies, G.G. Paulus, Vacuum birefringence at X-ray free-electron lasers. *New J. Phys.* **23**(9), 095001 (2021). <https://doi.org/10.1088/1367-2630/ac1df4>
10. B. Shen, Z. Bu, J. Xu, T. Xu, L. Ji, R. Li, Z. Xu, Exploring vacuum birefringence based on a 100 PW laser and an X-ray free electron laser beam. *Plasma Phys. Control Fusion* **60**(4), 044002 (2018). <https://doi.org/10.1088/1361-6587/aaa7fb>
11. Q. Yu, D. Xu, B. Shen, T.E. Cowan, H.-P. Schlenvoigt, X-ray polarimetry and its application to strong-field quantum electrodynamics. *High Power Laser Sci. Eng.* **11**, 71 (2023). <https://doi.org/10.1017/hpl.2023.45>
12. C.N. Danson, C. Haefner, J. Bromage, T. Butcher, J.-C.F. Chanteloup, E.A. Chowdhury, A. Galvanauskas, L.A. Gizzi, J. Hein, D.I. Hillier et al., Petawatt and exawatt class lasers worldwide. *High Power Laser Sci. Eng.* **7**, 54 (2019). <https://doi.org/10.1017/hpl.2019.36>
13. A.K. Harding, D. Lai, Physics of strongly magnetized neutron stars. *Rep. Prog. Phys.* **69**(9), 2631–2708 (2006). <https://doi.org/10.1088/0034-4885/69/9/R03>
14. IXPE. <https://ixpe.msfc.nasa.gov/index.html>
15. XPoSat. <https://www.isro.gov.in/XPoSat.html>
16. A. Santangelo, S. Zane, H. Feng, R. Xu, V. Doroshenko, E. Bozzo, I. Caiazzo, F.C. Zelati, P. Esposito, D. González-Caniulef, J. Heyl, D. Huppenkothen, G. Israel, Z. Li, L. Lin, R. Mignani, N. Rea, M. Orlandini, R. Taverna, H. Tong, R. Turolla, C. Baglio, F. Bernardini, N. Bucciantini, M. Feroci, F. Fürst, E. Göğüs, C. Güngör, L. Ji, F. Lu, A. Manousakis, S. Mereghetti, R. Mikusincova, B. Paul, C. Prescod-Weinstein, G. Younes, A. Tiengo, Y. Xu, A. Watts, S. Zhang, S.-N. Zhan, Physics and astrophysics of strong magnetic field systems with exp. *Sci. China Phys. Mech. Astron.* **62**(2) (2019). <https://doi.org/10.1007/s11433-018-9234-3>
17. Z. Wadiasingh, G. Younes, M.G. Baring, A.K. Harding, P.L. Gonthier, K. Hu, A.v.d. Horst, S. Zane, C. Kouveliotou, A.M. Beloborodov, C. Prescod-Weinstein, T. Chattopadhyay, S. Chandra, C. Kalapotharakos, K. Parfrey, D. Kazanas, Magnetars as astrophysical laboratories of extreme quantum electrodynamics: the case for a compton telescope. *Bull. Am. Astron. Soc.* **51**(3) (2019). <https://baas.aas.org/pub/2020n3i292>
18. G.G. Raffelt, *Stars as Laboratories for Fundamental Physics: the Astrophysics of Neutrinos, Axions, and Other Weakly Interacting Particles* (The University of Chicago Press, Chicago, 1996). <https://ui.adsabs.harvard.edu/abs/1996slfp.book.....R>
19. C.M. Kim, S.P. Kim, Magnetars as laboratories for strong field QED. *AIP Conf. Proc.* **2874**(1), 020013 (2024). <https://doi.org/10.1063/5.0215939>
20. S.L. Adler, Photon splitting and photon dispersion in a strong magnetic field. *Ann. Phys.* **67**(2), 599–647 (1971). [https://doi.org/10.1016/0003-4916\(71\)90154-0](https://doi.org/10.1016/0003-4916(71)90154-0)
21. W.-T. Ni, H.-H. Mei, S.-J. Wu, Foundations of classical electrodynamics, equivalence principle and cosmic interactions: a short exposition and an update. *Mod. Phys. Lett. A* **28**(03), 1340013 (2013). <https://doi.org/10.1142/S0217732313400130>
22. V.I. Denisov, B.N. Shvilkin, V.A. Sokolov, M.I. Vasili'ev, Pulsar radiation in post-Maxwellian vacuum nonlinear electrodynamics. *Phys. Rev. D* **94**(4), 045021 (2016). <https://doi.org/10.1103/PhysRevD.94.045021>
23. D.-H. Kim, C.M. Kim, S.P. Kim, Quantum refraction effects in pulsar emission. *Mon. Not. R. Astron. Soc.* **531**(1), 2148–2161 (2024). <https://doi.org/10.1093/mnras/stae1304>
24. S.E. Gralla, A. Lupsasca, A. Philippov, Pulsar magnetospheres: beyond the flat spacetime dipole. *Astrophys. J.* **833**(2), 258 (2016). <https://doi.org/10.3847/1538-4357/833/2/258>
25. W. Lockhart, S.E. Gralla, F. Özel, D. Psaltis, X-ray light curves from realistic polar cap models: inclined pulsar magnetospheres and multipole fields. *Mon. Not. R. Astron. Soc.* **490**(2), 1774–1783 (2019). <https://doi.org/10.1093/mnras/stz2524>
26. J. Kazmierczak, NASA's NICER Delivers Best-ever Pulsar Measurements, 1st Surface Map (2019). <https://www.nasa.gov/universe/nasas-nicer-delivers-best-ever-pulsar-measurements-1st-surface-map/>
27. C. Kalapotharakos, Z. Wadiasingh, A.K. Harding, D. Kazanas, The multipolar magnetic field of the millisecond pulsar psr j0030+0451. *Astrophys. J.* **907**(2), 63 (2021). <https://doi.org/10.3847/1538-4357/abcec0>
28. J. Petri, Theory of pulsar magnetosphere and wind. *J. Plasma Phys.* **82**(5) (2016). <https://doi.org/10.1017/S0022377816000763>
29. J.S. Heyl, N.J. Shaviv, Polarization evolution in strong magnetic fields. *Mon. Not. R. Astron. Soc.* **311**(3), 555–564 (2000). <https://doi.org/10.1046/j.1365-8711.2000.03076.x>
30. C. Wang, D. Lai, Wave modes in the magnetospheres of pulsars and magnetars. *Mon. Not. R. Astron. Soc.* **377**(3), 1095–1112 (2007). <https://doi.org/10.1111/j.1365-2966.2007.11531.x>
31. H. Kubo, R. Nagata, Determination of dielectric tensor fields in weakly inhomogeneous anisotropic media. II. *J. Opt. Soc. Am.* **71**(3), 327–333 (1981). <https://doi.org/10.1364/JOSA.71.000327>
32. H. Kubo, R. Nagata, Vector representation of behavior of polarized light in a weakly inhomogeneous medium with birefringence and dichroism. *J. Opt. Soc. Am.* **73**(12), 1719–1724 (1983). <https://doi.org/10.1364/JOSA.73.001719>
33. H. Kubo, R. Nagata, Vector representation of behavior of polarized light in a weakly inhomogeneous medium with birefringence and dichroism. II. Evolution of polarization states. *J. Opt. Soc. Am. A* **2**(1), 30–34 (1985). <https://doi.org/10.1364/JOSAA.2.000030>
34. J.S. Heyl, N.J. Shaviv, D. Lloyd, The high-energy polarization-limiting radius of neutron star magnetospheres—I. Slowly rotating neutron stars. *Mon. Not. R. Astron. Soc.* **342**(1), 134–144 (2003). <https://doi.org/10.1046/j.1365-8711.2003.06521.x>
35. J. Heyl, I. Caiazzo, Strongly magnetized sources: QED and X-ray polarization. *Galaxies* **6**(3), 76 (2018). <https://doi.org/10.3390/galaxies6030076>
36. O. Novak, M. Diachenko, E. Padusenko, R. Kholodov, Vacuum birefringence in the fields of a current coil and a guided electromagnetic wave. *Ukrain. J. Phys.* **63**(11), 979 (2018). <https://doi.org/10.15407/ujpe63.11.979>
37. D.-H. Kim, S. Trippe, General relativistic effects on pulsar radiation (2021). <https://arxiv.org/abs/2109.13387>
38. R.D. Blandford, D.G. Payne, Hydromagnetic flows from accretion discs and the production of radio jets. *Mon. Not. R. Astron. Soc.* **199**(4), 883–903 (1982). <https://doi.org/10.1093/mnras/199.4.883>
39. R.T. Gangadhara, On the method of estimating emission altitude from relativistic phase shift in pulsars. *Astrophys. J.* **628**, 923–930 (2005). <https://doi.org/10.1086/431138>
40. H. Euler, B. Kockel, Ueber die streuung von licht an licht nach der diracschen theorie. *Die Nat.* **23**(15), 246–247 (1935). <https://doi.org/10.1007/BF01493898>
41. G. Pavlov, O. Kargaltsev, B. M. Posselt Durant, X-ray observations of rotation powered pulsars (2013). https://www.cosmos.esa.int/documents/332006/943890/GPavlov_t.pdf
42. G. Hobbs, R.N. Manchester, L. Toomey, A. Kapur, ATNF Pulsar Catalogue (2024). <https://www.atnf.csiro.au/research/pulsar/psrcat>
43. D.A. Smith, S. Abdollahi, M. Ajello, M. Bailes, L. Baldini, J. Ballet, M.G. Baring, C. Bassa, J.B. Gonzalez, R. Bellazzini, A. Berretta, B. Bhattacharyya, E. Bissaldi, R. Bonino, E. Bottacini, J. Bregeon, P. Bruel, M. Burgay, T.H. Burnett, R.A. Cameron, F. Camilo, R.

- Caputo, P.A., Caraveo, E., Cavazzuti, G., Chiaro, S., Ciprini, C.J., Clark, I., Cognard, A., Corongiu, P.C., Orestano, M., Crnogorčević, A., Cuoco, S., Cutini, F., D'Ammando, A., de Angelis, M.E., DeCesar, S.D., Gaetano, R., de Menezes, J., Deneva, F., de Palma, N.D., Lalla, F., Dirirsa, L.D., Venere, A., Domínguez, D., Dumora, S.J., Fegan, E.C., Ferrara, A., Fiori, H., Fleischhack, C., Flynn, A., Franckowiak, P.C.C., Freire, Y., Fukazawa, P., Fusco, G., Galanti, V., Gammaldi, F., Gargano, D., Gasparri, F., Giacchino, N., Giglietto, F., Giordano, M., Giroletti, D., Green, I.A., Grenier, L., Guillemot, S., Guiriec, M., Gustafsson, A.K., Harding, E., Hays, J.W., Hewitt, D., Horan, X., Hou, F., Jankowski, R.P., Johnson, T.J., Johnson, S., Johnston, J., Kataoka, M.J., Keith, M., Kerr, M., Kramer, M., Kuss, L., Latronico, S.-H., Lee, D., Li, J., Li, B., Limyansky, F., Longo, F., Loparco, L., Lorusso, M.N., Lovellette, M., Lower, P., Lubrano, A.G., Lyne, Y., Maan, S., Maldera, R.N., Manchester, A., Manfreda, M., Marelli, G., Martí-Devesa, M.N., Mazziotta, J.E., McEnery, I., Mereu, P.F., Michelson, M., Mickaliger, W., Mitthumsiri, T., Mizuno, A.A., Moiseev, M.E., Monzani, A., Morselli, M., Negro, R., Nemmen, L., Nieder, E., Nuss, N., Omodei, M., Orienti, E., Orlando, J.F., Ormes, M., Palatiello, D., Paneque, G., Panzarini, A., Parthasarathy, M., Persic, M., Pesce-Rollins, R., Pillera, H., Poon, T.A., Porter, A., Possenti, G., Principe, S., Rainò, R., Rando, S.M., Ransom, P.S., Ray, M., Razzano, S., Razaque, A., Reimer, O., Reimer, N., Renault-Tinacci, R.W., Romani, M., Sánchez-Conde, P.M.S., Parkinson, L., Scotton, D., Serini, C., Sgrò, R., Shannon, V., Sharma, Z., Shen, E.J., Siskind, G., Spandre, P., Spinelli, B.W., Stappers, T.E., Stephens, D.J., Suson, S., Tabassum, H., Tajima, D., Tak, G., Theureau, D.J., Thompson, O., Tibolla, D.F., Torres, J., Valverde, C., Venter, Z., Wadiasingh, N., Wang, N., Wang, P., Wang, P., Weltevrede, K., Wood, J., Yan, G., Zaharijas, C., Zhang, W., Zhu, The third fermi large area telescope catalog of gamma-ray pulsars. *Astrophys. J.* **958**(2), 191 (2023). <https://doi.org/10.3847/1538-4357/acee67>
44. NIST: Digital Library of Mathematical Functions, National Institute of Standards and Technology, U.S. Department of Commerce (2024). <https://dlmf.nist.gov>
45. G.B. Rybicki, A.P. Lightman, *Radiative Processes in Astrophysics* (Wiley, New York, 1985). <https://doi.org/10.1002/9783527618170>. <https://cds.cern.ch/record/847173>
46. M.O. Scully, M.S. Zubairy, *Quantum Optics* (Cambridge University Press, Cambridge, 1997). <https://doi.org/10.1017/CBO9780511813993>. <http://ebooks.cambridge.org/ref/id/CBO9780511813993>
47. R. Taverna et al., Polarized X-rays from a magnetar. *Science* **378**(6620), 646–650 (2022). <https://doi.org/10.1126/science.add0080>
48. R. Turolla, R. Taverna, S. Zane, J. Heyl, IXPE observations of magnetar sources. *Galaxies* **12**(5), 53 (2024). <https://doi.org/10.3390/galaxies12050053>
49. D. Lai, Ixpe detection of polarized X-rays from magnetars and photon mode conversion at QED vacuum resonance. *Proc. Natl. Acad. Sci.* **120**(17) (2023). <https://doi.org/10.1073/pnas.2216534120>
50. R. Taverna, R. Turolla, D. Gonzalez Caniulef, S. Zane, F. Muleri, P. Soffitta, Polarization of neutron star surface emission: a systematic analysis. *Mon. Not. R. Astron. Soc.* **454**(3), 3254–3266 (2015). <https://doi.org/10.1093/mnras/stv2168>
51. I. Caiazzo, D. González-Caniulef, J. Heyl, R. Fernández, Probing magnetar emission mechanisms with X-ray spectropolarimetry. *Mon. Not. R. Astron. Soc.* **514**(4), 5024–5034 (2022). <https://doi.org/10.1093/mnras/stac1571>
52. J.A. Gil, J.K. Snakowski, Curvature radiation and the core emission of pulsars. *Astron. Astrophys.* **234**, 237–242 (1990). <https://ui.adsabs.harvard.edu/abs/1990A&A...234..237G>